GRACE 327-750

Gravity Recovery and Climate Experiment

Product Description Document for AOD1B Release 07

(Rev. 7.0, October 13, 2023)

Linus Shihora, Kyriakos Balidakis, Robert Dill,
Henryk Dobslaw

GFZ German Research Centre for Geosciences
Department 1: Geodesy

The data described in this document should be cited as:
Shihora, L., Balidakis, K., Dill, R., Dahle, C., Ghobadi-Far, K., Bonin, J., Dobslaw, H. (2022). Non-tidal background modeling for satellite gravimetry based on operational ECWMF and ERA5 reanalysis data: AOD1B RL07. Journal of Geophysical Research: Solid Earth, 127, e2022JB024360. https://doi.org/10.1029/2022JB024360

Contents

Document Changes Log

Issue	Date	Section	Description of Change
3.1	Apr 13, 2007		Last version that describes Releases 00 – 04 in full detail.
4.4	Dec 14, 2015		Last version that describes Release 05 in full detail as well as the various GAx Level-2 products required to account for offsets in AOD1B Releases 04 and 05 introduced by occasional ECMWF model changes.
6.2	May 30, 2018		Last version that describes Release 06 in full detail.
7.0	Oct 6, 2023		Fully revised document describing Release 07.

Chapter 1

Introduction

1.1 Overview on AOD1B Release 07

The Atmosphere and Ocean De-Aliasing Level-1B (AOD1B) product provides a priori information about temporal variations in the Earth's gravity field caused by global mass variability in atmosphere and ocean. It is based on analysis and forecast data out of the operational high-resolution global numerical weather prediction (NWP) model from the European Centre for Medium-Range Weather Forecasts (ECMWF) and ocean bottom pressure from an unconstrained simulation with the global ocean general circulation model MPIOM (Jungclaus *et al.*, 2013) that is consistently forced with ECMWF atmospheric data.

AOD1B provides fully normalized Stokes coefficients (Heiskanen & Moritz, 1967) of the anomalous external gravity field of the Earth caused by the mass variability predicted from those numerical models. It contains four different sets of coefficients: The effect of the atmosphere (**ATM**) that includes the contribution of atmospheric surface pressure over the continents; the static contribution of atmospheric pressure to ocean bottom pressure elsewhere; and the much weaker contribution of upper-air density anomalies above both continents and oceans. Further, the dynamic ocean contribution to ocean bottom pressure (**OCN**) is provided, and the sum of ATM and OCN are given as the so-called **GLO** coefficients, which are typically applied as a background model in precise orbit determination. For particular oceanographic applications, a fourth set of coefficients **OBA** is additionally included, which is zero over the continents and provides the simulated ocean bottom pressure that includes air and water contributions elsewhere. Thus, OBA deviates from GLO over the ocean domain only by disregarding the small contribution of upper-air density anomalies to the external gravity field. All anomalous signals given in AOD1B refer to corresponding long-term mean fields empirically estimated over the period 2007 – 2014.

The AOD1B product has a temporal sampling of 3 hours. Starting on Jan 1st 1975, atmospheric and oceanic pressure anomalies are expanded into Stokes coefficients up to degree and order (d/o) 180 to allow for a consistent processing of Starlette, LAGEOS and all other geodetic satellite missions equipped with laser retro-reflectors as well as specific low-Earth orbiting satellites designed for gravity field observations, most notably the CHAMP (Reigber *et al.*, 2002), GRACE (Tapley *et al.*, 2004), GOCE (Rummel *et al.*, 2011) and GRACE-FO (Landerer *et al.*, 2020) missions.

Periodic signals related to tides in the atmosphere and its corresponding oceanic response have been empirically estimated and removed from the non-tidal time-series of AOD1B RL07. This includes 16 tidal constituents in the diurnal, semi-diurnal and ter-diurnal frequency bands.

The non-tidal AOD1B coefficients are routinely updated every day and all files are made available via the GRACE data archives. Up-to-date information on AOD1B is provided via the web-page

http://www.gfz-potsdam.de/en/esmdata. The current release of AOD1B has been extensively validated by means of GRACE-FO K-band laser-ranging pre-fit residuals, GRACE-FO LRI pre-fit residuals and high-pass filtered satellite altimetry-based sea-level anomalies. Details are provided in the following research article:

- Shihora, L., Balidakis, K., Dill, R., Dahle, C., Ghobadi-Far, K., Bonin, J., Dobslaw, H. (2022). Non-tidal background modeling for satellite gravimetry based on operational ECWMF and ERA5 reanalysis data: AOD1B RL07. Journal of Geophysical Research: Solid Earth, 127, e2022JB024360. 10.1029/2022JB024360.
- Shihora, L., Balidakis, K., Dill, R., Dobslaw, H. (2023): Assessing the stability of AOD1B atmosphere-ocean non-tidal background modelling for climate applications of satellite gravity data: long-term trends and 3-hourly tendencies. - Geophysical Journal International, 243, 2, 1063-1072. 10.1093/gji/ggad119.

1.2 Relevance of AOD1B for Satellite Gravimetry

Gravity field determination from low Earth-orbiting satellites is generally affected by time-changes in the external gravitational field and its underlying mass distribution within the atmosphere, at the surface, and in the Earth's interior. Due to sampling limitations of polar-orbiting satellite missions, observations are typically accumulated over a certain time-period in order to be able to solve for a global gravity field solution with reasonably high spatial resolution. For the GRACE mission, typical accumulation times range between 7 and 30 days.

Besides tidal signals that are particularly present in the oceans and in the solid Earth, there are also substantial non-tidal mass variations at periods below 30 days that take place in the vicinity of the Earth's surface. Evolving synoptic weather systems with horizontal dimensions of several hundred kilometers that are advected with the mean flow cause surface pressure changes of a few $\sim$10 hPa at moderate latitudes. Heavy precipitation events associated with convective processes might cause occasionally a rapid increase of the amount of water stored on the continents, and surface winds associated with cyclonic pressure systems lead to a redistribution of oceanic water masses, and thus changes in ocean bottom pressure.

Failure to account for those high-frequency signals within the gravity field retrieval process causes temporal aliasing of such signals into the estimated monthly-mean gravity fields, a process that contributes to the systematic meridional striations common to all un-regularized GRACE gravity field solutions. Although this high-frequency variability is also affecting gravity field models from CHAMP and GOCE satellite observations, the GRACE mission, dedicated to the observation of time-variable mass transport phenomena, is particularly affected up to intermediate spatial wavelengths of several hundred kilometers.

Satellite gravimetry is set apart from all other currently operating satellite remote sensing systems by the fact that it is not only sensitive to the atmospheric composition or some surface properties of the Earth, but to changes in the global mass distribution independently of its surface exposure. GRACE is therefore particularly capable of providing quantitative estimates of water mass anomalies in all possible storage compartments including surface water, snow pack, continental ice, soil moisture, and the deep aquifers. At the same time, GRACE is inherently insensitive to discriminate vertically between those storages: in order to separate between mass anomalies in the atmosphere and underneath, prior information on atmospheric mass variability is required.

To meet those two purposes — the removal of high-frequency mass variability to avoid temporal aliasing, and the provision of prior information on atmospheric mass variability to allow for signal separation over the continents — AOD1B should fulfil the following minimal requirements:

- AOD1B needs to be provided with very high temporal and spatial resolution to properly represent transient atmospheric weather systems and their associated pressure and mass signatures.
- AOD1B needs to be stable on long time-scales from years to decades in order to avoid the introduction of spurious low-frequency signals or discontinuities into the GRACE gravity fields that are subsequently prone to be interpreted erroneously in an entirely different geophysical context.

1.3 History of Available AOD1B Releases

Release 00 of AOD1B is available for the period July 2000 until April 2003 and incorporates operational ECMWF analysis data and ocean bottom pressure simulated with the barotropic ocean model PPHA (Hirose *et al.*, 2001). Only the combined effect of atmospheric and oceanic mass variability is provided, and a mean field calculated over the year 2001 has been subtracted. Signals from atmospheric tides and the simulated oceanic response are fully retained in those coefficients.

Release 01 is available for the period July 2000 until June 2007 and is identical with release 00 except for the fact that separate coefficients for atmosphere and ocean are now provided.

Release 02 consists of a short test series of ocean bottom pressure from an improved version of PPHA that has been calculated for only eight selected months within the period May 2003 until January 2005. The signature of the atmospheric tide S_2 has been removed from the surface pressure grids based on a climatology provided by Ray & Ponte (2003) before forcing PPHA in order to avoid a double book-keeping of the oceanic S2 which is also part of the ocean tide background model typically applied in the GRACE orbit determination. The S_2 signal in the atmosphere, however, is still included in the 6 hourly coefficients, even though it is partially aliased into a standing wave pattern. All anomalies given in AOD1B RL02 do now refer to mean values estimated over the period 2001 – 2002.

Release 03 is based on an early simulation with an OMCT configuration discretized on a 1.875° latitude-longitude grid (Thomas & Dobslaw, 2004). The ocean simulation also predicts seasonal variations in total ocean mass and thus barystatic sea-level changes during 2002 – 2004, which have been found to be less reliable when compared to observations. Since January 1st, 2005, total ocean mass in RL03 is therefore fixed to a constant at all time-steps. Users of GRACE gravity fields from GFZ RL03 and JPL RL02 are referred to GRACE Technical Note #4 (Bettadpur *et al.*, 2006) for further information. Release 03 AOD1B is available until January 2007.

A first long-term simulation from OMCT with updated momentum transfer parametrization is the basis for AOD1B **release 04** (Dobslaw & Thomas, 2007). OMCT has been forced with ERA-40 atmospheric re-analysis data (Uppala *et al.*, 2005) for the time-period January 1976 until December 2000, followed by simulations forced with operational ECMWF analyses so that it is also suitable for the consistent re-processing of historical satellite laser ranging observations (Flechtner *et al.*, 2008). The product contains for the first time an additional set of coefficients of ocean bottom pressure variability (OBA) that disregards the contribution of upper-air density anomalies for oceanographic applications. The mean fields removed are once more calculated from the years 2001 and 2002. Release 04 has been processed until April 2012.

The **release 05** was introduced in 2012. The series is based on OMCT discretized on a 1.0° latitude-longitude grid (Dobslaw *et al.*, 2013), that has been integrated with ERA-Interim reanalysis data (Dee *et al.*, 2011) for the time-period January 1979 to December 2000, followed by simulations forced with operational ECMWF analyses. The atmospheric data processing has not been changed since release 04. Corresponding mean fields calculated over the years 2001 – 2002 are once more

subtracted. Until release 05, all versions of AOD1B have 6 hourly temporal resolution and are expanded up to d/o = 100. Release 05 is available until the end of the year 2017.

Release 06 was made available in the year 2016 and covers the years 1976 to at least 2023. It was based on the ERA-40 reanalysis for 1976-1978 (Uppala *et al.*, 2005), ERA-Interim reanalysis from 1979 – 2006 (Dee *et al.*, 2011) and the operational ECMWF analyses for all subsequent years. Surface pressure fields have been mapped to a common reference orography for consistency. The oceanic component is based on simulations with the Max-Planck-Institute for Meteorology Ocean Model (MPIOM; Jungclaus *et al.*, 2013) forced with the corresponding atmospheric data. All mass anomalies were computed with respect to a mean field computed over the years 2003 – 2014. RL06 featured a temporal resolution of 3h and is expanded up to d/o 100 and 180 before and after the year 2000, respectively.

The present document is describing AOD1B **release 07** that was introduced in the year 2022. For further information on older versions of AOD1B, please refer to the previous AOD1B Product Description Documents that are available from the GRACE archives.

Chapter 2

Atmospheric Surface Pressure Variability

2.1 Atmospheric Data-Sets Available From ECMWF

The atmospheric component of AOD1B is based on operational and re-analysis data from the ECMWF. The ERA5 reanalysis (Hersbach *et al.*, 2020) is used for all years until 2017. From 2018 onwards operational data from the ECMWF is used. Operational NWP data-sets are available for the whole time-period as well, but their quality is drastically improving in particular in the most recent years due to increased spatial resolution, improved representation of physics in the model, and tremendous progress in data assimilation due to the computing resources available today.

Analysis data is assumed to be the most precise representation of the state of the atmosphere. With the transition to operational ECMWF data, however, we take advantage of the low-latency availability of the atmospheric data. The combination between analysis and forecasts is performed as suggested by Dobslaw & Thomas (2005) to arrive at a 3-hourly temporal resolution.

In the following sections, only the contribution of atmospheric surface pressure to changes in the external gravity field of the Earth is considered. Effects of density anomalies in upper-air layers of the atmosphere are calculated separately as described in Ch. 4.

2.2 Reduction of Pressure to Reference Orography

Atmospheric pressure decreases exponentially with altitude. As a rule of thumb, surface pressure at mean sea-level changes by 1 hPa — which approximately corresponds to 1 cm equivalent water height — every 8 m. Thus, atmospheric surface pressure from different numerical models need to refer to the same geopotential height before it can be compared to each other or combined into one time-series.

For the reduction of atmospheric surface pressure to a reference orography, we make use of ECMWF's sea-level pressure diagnostic that has been kindly made available in form of a set of FORTRAN routines, that we have adapted in order to run it independently of ECMWF's Integrated Forecast System (IFS). Within those routines, mean sea-level pressure p_{msl} is calculated as follows (Yessad, 2015):

$$p_{\mathrm{msl}} = p_s \exp\left\{ \frac{\Phi_s}{R_d T_s} \left[1 - \frac{\alpha \Phi_s}{2 R_d T_s} + \frac{1}{3} \left(\frac{\alpha \Phi_s}{R_d T_s} \right)^2 \right] \right\}. \tag{2.1}$$

Here, p_s is atmospheric surface pressure, Φ_s is the surface geopotential, R_d is the gas constant for dry air, and T_s the surface virtual temperature extrapolated from the lowest model level *nlev* according to

$$T_s = T_{\text{nlev}} + \alpha T_{\text{nlev}} \left(\frac{p_s}{p_{\text{nlev}}} - 1 \right), \tag{2.2}$$

with a temperature reduction factor α,

$$\alpha = \Gamma R_d / g_{\text{WMO}}, \tag{2.3}$$

where $\Gamma = 6.5$ K/km is the standard temperature lapse rate, and $g_{\text{WMO}} = 9.80665$ m/s^2 the standard gravity acceleration according to the definitions of the World Meteorological Organization. Both surface temperatures and the temperature lapse rate are slightly modified for altitudes above 2000 m and extreme surface temperatures in order to avoid extrapolation to too low pressures over high and warm surfaces, and also to too high pressures over very cold surfaces; the details are given in Yessad (2015).

In addition to reducing atmospheric surface pressure to mean sea-level, the algorithm is generally applicable to extrapolate pressure vertically to arbitrary heights. For AOD1B RL07, the orography of IFS version 41r1 — which was in operation at ECMWF between May 12th, 2015 and March 8th, 2016 — is chosen as a reference orography, where all surface pressure data-sets are reduced to. In case that this reference orography is locally higher than the model orography, pressure is interpolated from the nearest model levels that are obtained from integrating virtual temperatures and thus geopotential heights vertically upwards.

2.3 ECMWF Model Changes Relevant for AOD1B

The earlier years of RL07 up to 2017 are based on ERA5 reanalysis data which is based on IFS cycle 41r2. Operational model data from ECMWF is used to compute AOD1B RL07 coefficients from January 1st, 2018 onwards. At this time, cycle 43r3 was in operation, whereas at the time of publication of AOD1B RL07 it was already cycle 47r3. A full documentation of changes to the operational NWP model from ECMWF is available from `www.ecmwf.int/en/forecasts/documentation-and-support/changes-ecmwf-model` and we briefly mention a subset of modifications only that are most relevant for AOD1B.

- **January 1st, 1975**: ERA5 is used to process the AOD1B coefficients. It utilizes cycle 41r2 of the IFS with a N320 spatial resolution ($\sim$ 31 km) and 137 vertical sigma layers. Analysis data is obtained from 4D-Var assimilation windows with a length of twelve hours each day.
- **January 1st, 2018**: Operational ECMWF data is employed for AOD1B RL07 for the first time with cycle 43r3 with a horizontal O1280 grid ($\sim$ 9 km) and 137 levels. The data assimilation is still based on 12-hourly 4D-Var windows.

2.4 Static Contribution of the Atmosphere to Ocean Bottom Pressure

Ocean-bottom pressure is commonly regarded as the summed effect of the hydrostatic pressure from both the atmospheric and oceanic masses situated along the plumb line above a certain position

of the sea-floor. For the representation of global bottom pressure in model data-sets, those masses are traditionally separated into an atmospheric and an oceanic contribution. The local sea-surface, however, reacts rapidly to changes in atmospheric surface pressure. As evidenced from the analysis of global sea-level variations observed with satellite altimetry, the ocean is adjusting almost perfectly to surface pressure changes at periods of a few days and longer (Wunsch & Stammer, 1997). Thus, atmospheric and oceanic contributions to ocean-bottom pressure are highly anti-correlated, and largely cancel each other when added.

To remove the correlation between the atmospheric and oceanic components of ocean-bottom pressure, we only include the static contribution of the atmosphere to ocean bottom pressure into the ATM coefficients. Technically, this implies replacing the surface pressure at every grid point over the oceans with the area-mean surface pressure averaged over the whole ocean domain as defined by the AOD1B land-sea mask:

$$p'_s(\theta,\phi) = \begin{cases} p_s(\theta,\phi) & \text{at the continents} \\ \dfrac{1}{A_{\text{Oceans}}} \iint\limits_{\text{Oceans}} p_s(\theta,\phi)dA & \text{over the oceans} \end{cases} \tag{2.4}$$

The C_{00} estimates of ATM are not affected by this inverse-barometric (IB) correction, but the temporal variability of several low-degree spherical harmonics reduces substantially. Note that tidal signals in the atmosphere have been estimated and subtracted prior to the replacement of pressure with its area-mean value over the oceans. Further details on the handling of atmospheric tides in AOD1B are provided in Ch. 5.

2.5 Atmospheric Surface Pressure Contributions to the Time-Variable Gravity Field

Fundamentals

We rely in the following on the formalism of Boy & Chao (2005) that itself builds on previous work of Wahr *et al.* (1998) and Swenson & Wahr (2002). The time-variable external gravity field of the Earth as expressed in terms of deviations in geoid height $\Delta\xi(\theta,\phi)$ from a certain reference state can be conveniently expanded in spherical harmonics:

$$\Delta\xi(\theta,\phi) = a_{45} \sum_{l=0}^{\infty} \sum_{m=0}^{l} \tilde{P}_{lm}(cos\theta)\{\Delta C_{lm} \cos m\phi + \Delta S_{lm} \sin m\phi\} \tag{2.5}$$

Here, a_{45} is the Earth's mean radius, θ is colatitude, ϕ longitude, $\tilde{P}_{lm}$ are fully normalized associated Legendre Functions, and ΔC_{lm}, ΔS_{lm} are dimensionless Stokes coefficients. Note that in this section the time-dependency of ΔC_{lm}, ΔS_{lm} and $\Delta\xi$ has been omitted to improve readability. The Stokes coefficients are related to anomalies in the Earth's density distribution:

$$\Delta C_{lm} = \frac{3}{4\pi a_{45}\rho_E} \frac{1}{2l+1} \int_0^{2\pi} \int_0^{\pi} \Delta I_l(\theta,\phi) \tilde{P}_{lm}(\cos\theta) \cos m\phi \, \sin\theta \, d\theta d\phi \tag{2.6}$$

$$\Delta S_{lm} = \frac{3}{4\pi a_{45}\rho_E} \frac{1}{2l+1} \int_0^{2\pi} \int_0^{\pi} \Delta I_l(\theta,\phi) \tilde{P}_{lm}(\cos\theta) \sin m\phi \, \sin\theta \, d\theta d\phi \tag{2.7}$$

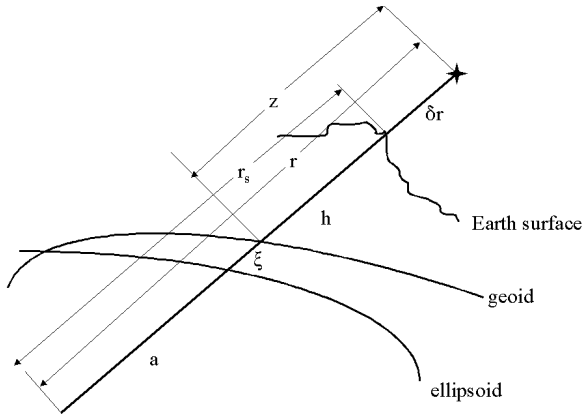

Figure 2.1: Radial coordinates employed to characterize the vertical position of pressure and density anomalies that contribute to the time-variable Earth's gravity field: ellipsoidal radius a, geoid height ξ, orthometric height of the surface of the orography h, and the orthometric height of any point above the orography $z = h + \delta r$.

where ρ_E is the average density of the Earth, and ΔI_l denotes the change in the so-called "inner integral" over all masses in the Earth System in radial direction:

$$\Delta I_l(\theta, \phi) = \int_0^\infty \left(\frac{r}{a_{45}}\right)^{l+2} \Delta\rho(r, \theta, \phi) dr \tag{2.8}$$

with $\Delta\rho(r, \theta, \phi)$ denotes a density anomaly at a certain height r which might reside anywhere between the centre of the Earth at $r = 0$ and the top of the atmosphere.

Radial Coordinates

The radial coordinate r of eq. 2.8 for a given mass element is taken in the following as the sum of the ellipsoidal radius $a(\theta)$, the geoid height ξ, the orthometric height of the orography h, and the orthometric height of any point above the orography $z = h + \delta r$ (Fig. 2.1):

$$r(\theta, \phi) = a(\theta) + \xi(\theta, \phi) + h(\theta, \phi) + \delta r(\theta, \phi) \tag{2.9}$$
$$= a(\theta) + \xi(\theta, \phi) + z(\theta, \phi) \tag{2.10}$$

For the calculation of AOD1B, the (time-invariant) geoid undulations ξ are entirely omitted since those vary globally only in the range of ±120 m. The ellipsoidal radius $a(\theta)$ is calculated from the reference ellipsoid given in the IERS conventions 2010 (Petit & Luzum, 2010), and orthometric heights z are derived from the reference orography introduced above by means of a transformation from geopotential heights H as given by Boy & Chao (2005):

$$z = (1 - 0.002644 \cos 2\theta)H + (1 - 0.0089 \cos 2\theta)\frac{H^2}{6.245 \cdot 10^6} \tag{2.11}$$

Spatially Variable Gravity

In atmospheric modelling, the gravitational acceleration g is typically set to a constant value as defined by the World Meteorological Organization (WMO):

$$g_{\mathrm{WMO}} = 9.80665\ m/s^2 \tag{2.12}$$

In the calculation of AOD1B, we employ normal gravity $g(\theta, z)$ based on the GRS80 reference system as defined in the IERS conventions (Petit & Luzum, 2010) with

$a_0 = 6378136.6\ m$ semi-major axis, and
$1/f = 298.25642$ flattening factor.

The mean radius of the Earth a_{45} introduced above is taken as the corresponding ellipsoidal radius at 45° latitude.

Thin-Layer Approximation to the Inner Integral

In the simplest case, all mass variability in the Earth's system that causes changes in the gravity field is concentrated within a shell of infinite thickness so that it can be characterized by a surface pressure anomaly. In that case, eq. 2.8 simplifies to (Swenson & Wahr, 2002):

$$\Delta I_l(\theta,\phi) = \Big(\frac{a(\theta)+h(\theta,\phi)}{a_{45}}\Big)^{l+2} \int_{\text{thin layer}} \rho dr = \Big(\frac{a(\theta)+h(\theta,\phi)}{a_{45}}\Big)^{l+2} \frac{\Delta p_s(\theta,\phi)}{g(\theta,z)}, \tag{2.13}$$

which only depends on the surface pressure anomaly $\Delta p_s(\theta,\phi)$, the vertical position of that anomaly $a(\theta)+h(\theta,\phi)$ and the corresponding gravity acceleration.

Numerical Implementation

The inner integral of eq. 2.13 is obtained from atmospheric surface pressure anomalies after mapping to a common reference orography, de-tiding, replacement of pressure at ocean grid points with its area-mean value, and subtraction of a long-term mean field as derived from the period 2007 – 2014. This (degree-dependent) field is regarded as a quasi-continuous function $f(\theta,\phi)$ on the sphere which is subsequently analysed into fully normalized spherical harmonic coefficients with the algorithm published by Wang *et al.* (2006):

$$f_{lm} = \int_\sigma f(\theta,\phi)\, Y^*(\theta,\phi)\, d\sigma \tag{2.14}$$

where (θ,ϕ) are colatitude and longitude and $Y^*(\theta,\phi)$ the conjugate complex surface spherical harmonics of degree l and order m:

$$Y^*_{lm}(\theta,\phi) = (-1)^m \sqrt{\frac{2\,l+1}{4\,\pi}\frac{(l-m)!}{(l+m)!}}\, P_{lm}(\cos\theta)\, e^{im\phi} \tag{2.15}$$

The approach is suitable to analyse non-smooth data with discontinuous slopes that are discretized on equal-angular or Gaussian grids. Discontinuities in surface pressure anomalies may in particular occur in regions of mountain ridges or at the coastlines, so that the method is well suited for our purposes.

The data have to be given in a defined domain of $\theta_a \le \theta \le \theta_b$ and $\phi_a \le \phi \le \phi_b$ and the grid is equally spaced in longitude and latitude direction with the sampling intervals $\Delta\theta$ and $\Delta\phi$. The grid cells are defined by the node rows from 0 at $\theta = \theta_a$ to $i_{\max}$ at $\theta = \theta_b$ and the node columns from 0 at $\phi = \phi_a$ to $j_{\max}$ at $\phi = \phi_b$. Equation 2.14 is then discretized as follows:

$$f_{lm} = \sum_{i=1}^{i_{\max}} \sum_{j=1}^{j_{\max}} \int_{\sigma_{ij}} f(\theta,\phi)\, Y^*_{lm}(\theta,\phi)\, d\sigma \tag{2.16}$$

The values of $f(\theta,\phi)$ for a specific grid cell are obtained from a bilinear function:

$$f(\theta,\phi) = f(x,\phi) = A_{ij}\, x + B_{ij}\, \phi + C_{ij}\, x\, \phi + D_{ij} \tag{2.17}$$

with the notation $x = \cos\theta$. The interpolation coefficients (A_{ij}, B_{ij}, C_{ij}, and D_{ij}) are determined with function values of the four node points of each grid cell; see Wang *et al.* (2006, eq. 13) for the explicit integration coefficients. Those are included in eq. 2.16 to obtain the final equation for the analysis of the spherical harmonic coefficients:

$$\begin{aligned} f_{lm} = {} & (-1)^{m+1} \sqrt{\frac{2\,l+1}{4\,\pi}} \sum_{i=1}^{i_{\max}} \left[\int_{x_{i-1}}^{x_i} x \sqrt{\frac{(l-m)!}{(l+m)!}}\, P_{l,m}(x)\, dx \right] \sum_{j=1}^{j_{\max}} \left\{ \int_{\phi_{j-1}}^{\phi_j} (A_{ij} + C_{ij}\,\phi)\, e^{-im\phi}\, d\phi \right\} \\ & + (-1)^{m+1} \sqrt{\frac{2\,l+1}{4\,\pi}} \sum_{i=1}^{i_{\max}} \left[\int_{x_{i-1}}^{x_i} \sqrt{\frac{(l-m)!}{(l+m)!}}\, P_{l,m}(x)\, dx \right] \sum_{j=1}^{j_{\max}} \left\{ \int_{\phi_{j-1}}^{\phi_j} (D_{ij} + B_{ij}\,\phi)\, e^{-im\phi}\, d\phi \right\} \end{aligned} \tag{2.18}$$

The integration over the longitude in the curly braces is solved via the Fast Fourier Transform. The integration over the latitude in the square braces is solved by using recursion relations for the Legendre Polynomials. Those recursion relations are stable up to degree and order 2200 for double precision calculations. A detailed description of the whole algorithm is given in Wang *et al.* (2006).

The estimated surface spherical harmonic coefficients are subsequently transformed into fully normalized surface spherical harmonics by the relation:

$$\begin{aligned} c_{l0} &= \frac{1}{\sqrt{4\,\pi}}\, f_{l0}, && (m = 0) \\ c_{lm} &= \frac{(-1)^m}{\sqrt{2\,\pi}}\, \mathrm{Re}(f_{lm}), && (m > 0) \\ s_{lm} &= \frac{(-1)^{m+1}}{\sqrt{2\,\pi}}\, \mathrm{Im}(f_{lm}), && (m > 0) \end{aligned} \tag{2.19}$$

In a last step, the potential coefficients are obtained out of the mass coefficients following Dong *et al.* (1996):

$$\begin{Bmatrix} C_{lm} \\ S_{lm} \end{Bmatrix} = 4\,\pi\, \frac{a_{45}^2}{M_E} \left(\frac{1 + k_l'}{2\,l+1} \right) \begin{Bmatrix} c_{lm} \\ s_{lm}. \end{Bmatrix} \tag{2.20}$$

In addition to the direct effect of surface masses, the elastic deformations of the solid Earth under the variable mass load are taken into account in eq. 2.20 via the Load Love numbers k_l'. We use numerical estimates calculated by Pascal Gegout given in the Center of Mass of the Earth System (CM) frame for the PREM Earth model (Tab. 2.1). In order to properly represent degree-1 information from the atmospheric surface mass variability, we additionally calculate the k_1 Load Love number for the CF frame following Blewitt (2003):

$$\left[1 + k_1'\right]_{CF} = \left[-\frac{1}{3}\, h_1' - \frac{2}{3}\, l_1' \right]_{CM} \tag{2.21}$$

2.6 Spatial Patterns of Trends and Variabilities

Stokes coefficients of the atmospheric surface pressure contribution to the time-variations of the Earth's gravity field have been analysed every 3 hours for the period 1975 until 2021. Subsequently, those coefficients are synthesized back onto an equi-angular grid for a series of consistency assessments as reported below. For simplicity, all anomalies in the potential are always expressed in terms of equivalent surface pressure (Wahr *et al.*, 1998):

$$p_{\mathrm{resynt}}(\theta,\phi) = g_{\mathrm{WMO}}\Delta\sigma(\theta,\phi) \tag{2.22}$$

$$= g_{\mathrm{WMO}}\frac{a_{45}\rho_{ave}}{3}\sum_{l=0}^{\infty}\sum_{m=0}^{l}\frac{2l+1}{1+k_l'}\tilde{P}_{lm}(\cos\theta)\left(\Delta C_{lm}\cos m\phi + \Delta S_{lm}(m\phi)\right) \tag{2.23}$$

where a spherical geometry with the Earth's mean radius a_{45} and a constant gravity acceleration g_{WMO} have been applied.

Atmospheric surface pressure variations utilized for AOD1B do not include strong trends (Fig. 2.2). During the 45-years long period between 1975 – 2020, local atmospheric pressure changes by less than 5 Pa a^{-1}, which corresponds to a change of only 5 mm water equivalent during one decade. Such tiny pressure drifts are well within the range of natural climate variability. Apparent trends estimated over the GRACE mission period 2002 – 2020 approach 15 Pa a^{-1} in several regions of the world, but are in fact not related to long-term drifts in pressure but to interannual-to-decadal climate variability.

The yearly mean signals of atmospheric surface pressure are in the range of about 5 hPa (Fig. 2.3). The spatial pattern is dominated by large-scale features as previously known from climate model simulations. Annual mean pressure anomalies of 3 to 5 hPa in Antarctica, however, underline once more the importance of high-quality long-term stability of AOD1B, since ice-mass change signals in that area are of similar or even smaller magnitude.

Standard deviations of the 3 hourly atmospheric surface pressure anomalies calculated individually between 2002 and 2018 do not reveal systematic changes in variability during the years (Fig.2.4).

Table 2.1: Elastic Load Love Numbers $k_l^{'}$ for the PREM Earth model.

l	$k_l^{'}$
0	+0.000
1	+0.026
2	-0.305
3	-0.196
4	-0.134
5	-0.105
6	-0.090
7	-0.082
8	-0.077
9	-0.072
10	-0.069

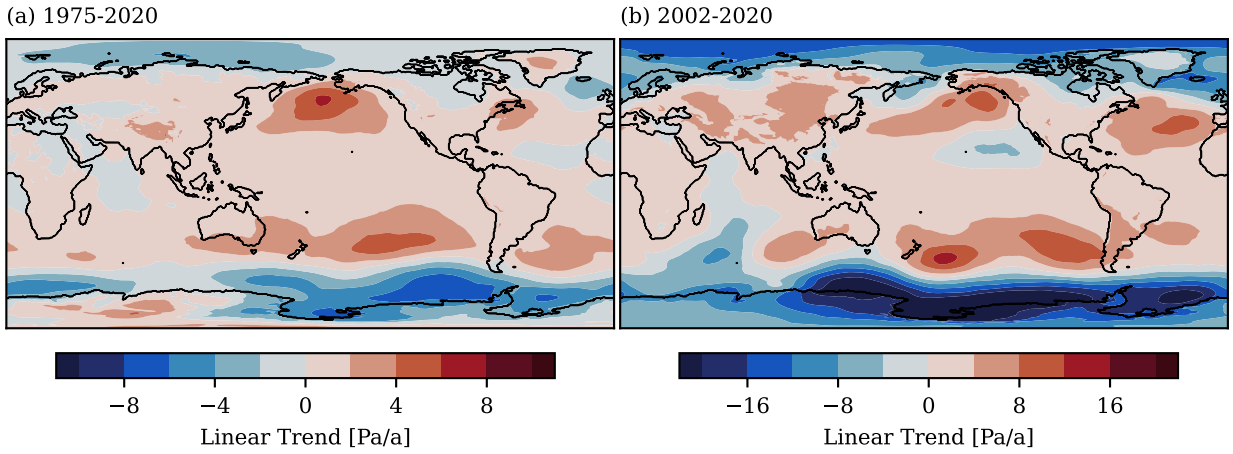

Figure 2.2: Trend in ERA5 and operational ECMWF data based atmospheric surface pressure for 1975 – 2020 (a) and 2002 – 2020 (b) as included in AOD1B RL07

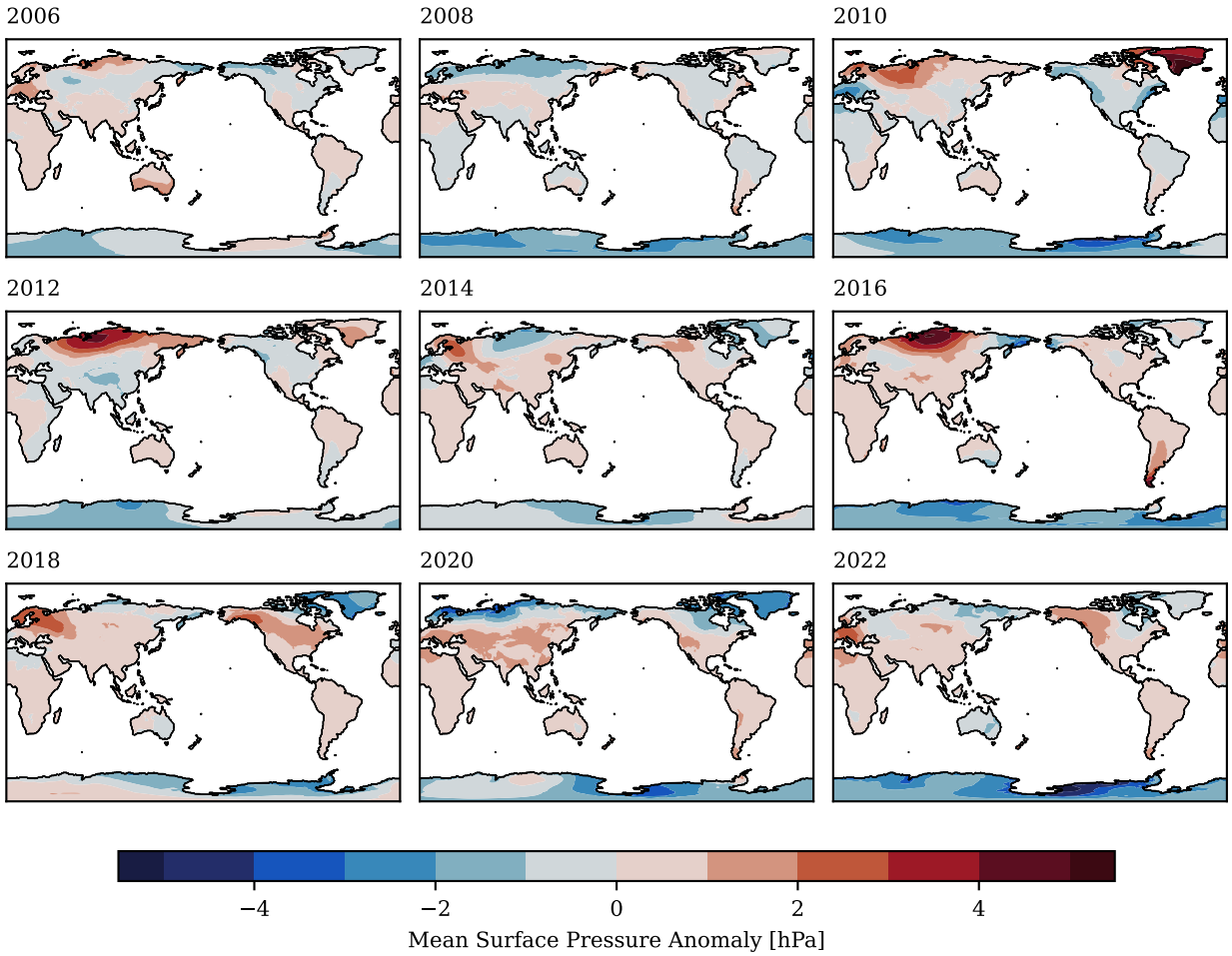

Figure 2.3: Yearly means of atmospheric surface pressure anomalies for the years 2006 – 2022 as included in AOD1B RL07.

Surface pressure changes are strongest in moderate-to-high latitudes at both hemispheres. Vari-

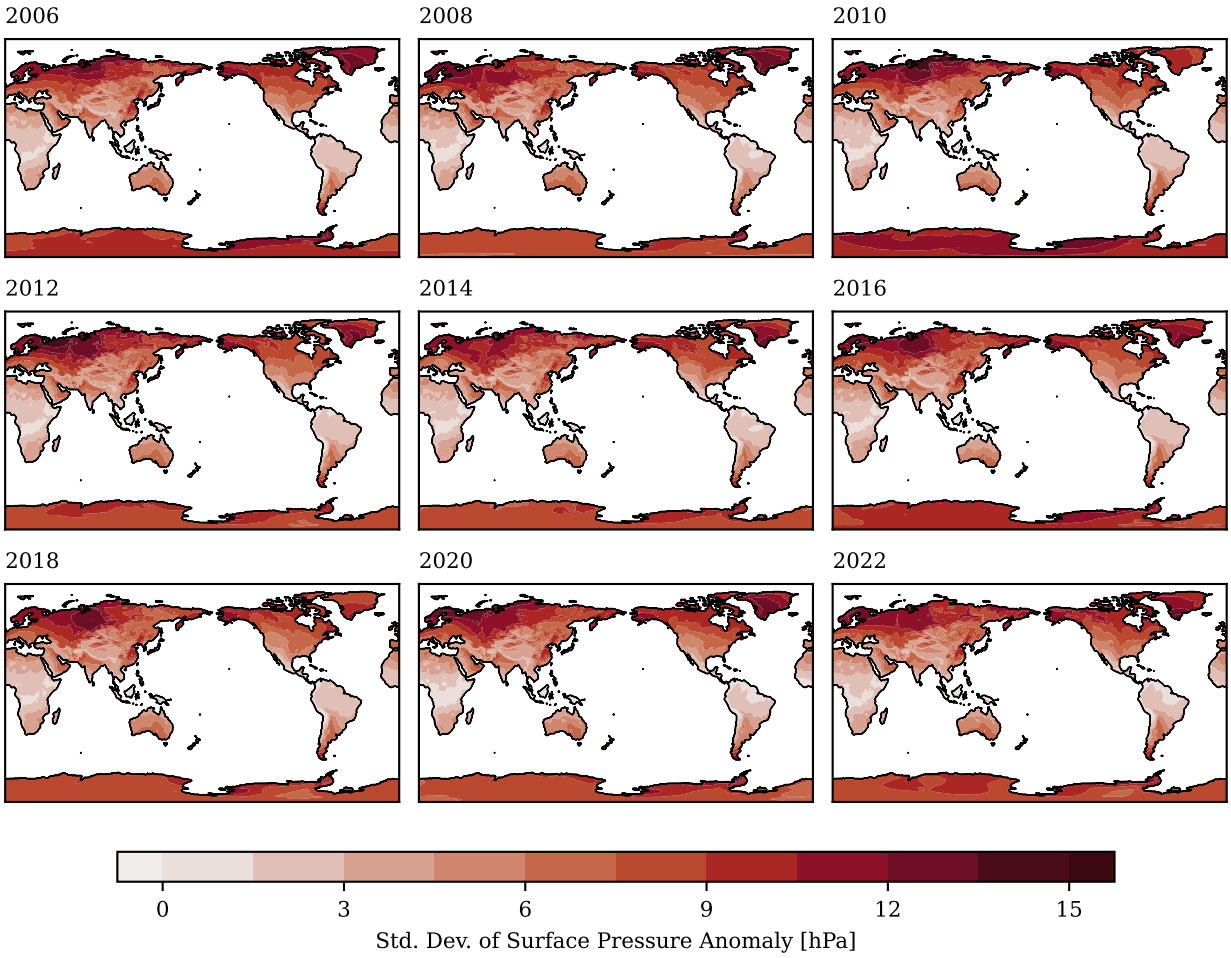

Figure 2.4: Standard deviation of 3 hourly atmospheric surface pressure anomalies as included in AOD1B RL07 calculated individually for the years 2006 – 2022.

ability pattern are clearly modified by orographic features as the Andes, Himalayas, Karakoram, or the Ural, but no apparent effects of the ECMWF model resolution changes are evident.

2.7 Assessment of 3-Hourly Tendencies

We also calculate differences of consecutive 3-hourly time-steps of the anomalies in the gravity potential expressed in terms of equivalent surface pressure. Those tendencies will be particularly large at times where a jump in the series appears. However, neither the yearly standard deviations of the surface pressure tendencies (Fig. 2.5) nor the time-series of area-averaged absolute values of pressure tendencies (Fig. 2.6) give evidence for such inconsistencies. The only notable feature is a much higher variability in the tendencies in the earliest years of AOD1B RL07, namely 1975 – 1978. The earliest years of surface pressure data are based on the so-called back extension of the ERA5 re-analysis. As described in Bell *et al.* (2021), there is significant improvements in the quality of surface pressure data with the introduction of the TIROS Operational Vertical Sounder (TVOS) satellite data in 1979. Before that, variations in surface pressure are larger. While the impact is likely small in applications of ADO1B, the relatively lower accuracy of the ERA5 Back Extension based years in AOD1B should be kept in mind when using the background model data spanning the years 1975 – 1978.

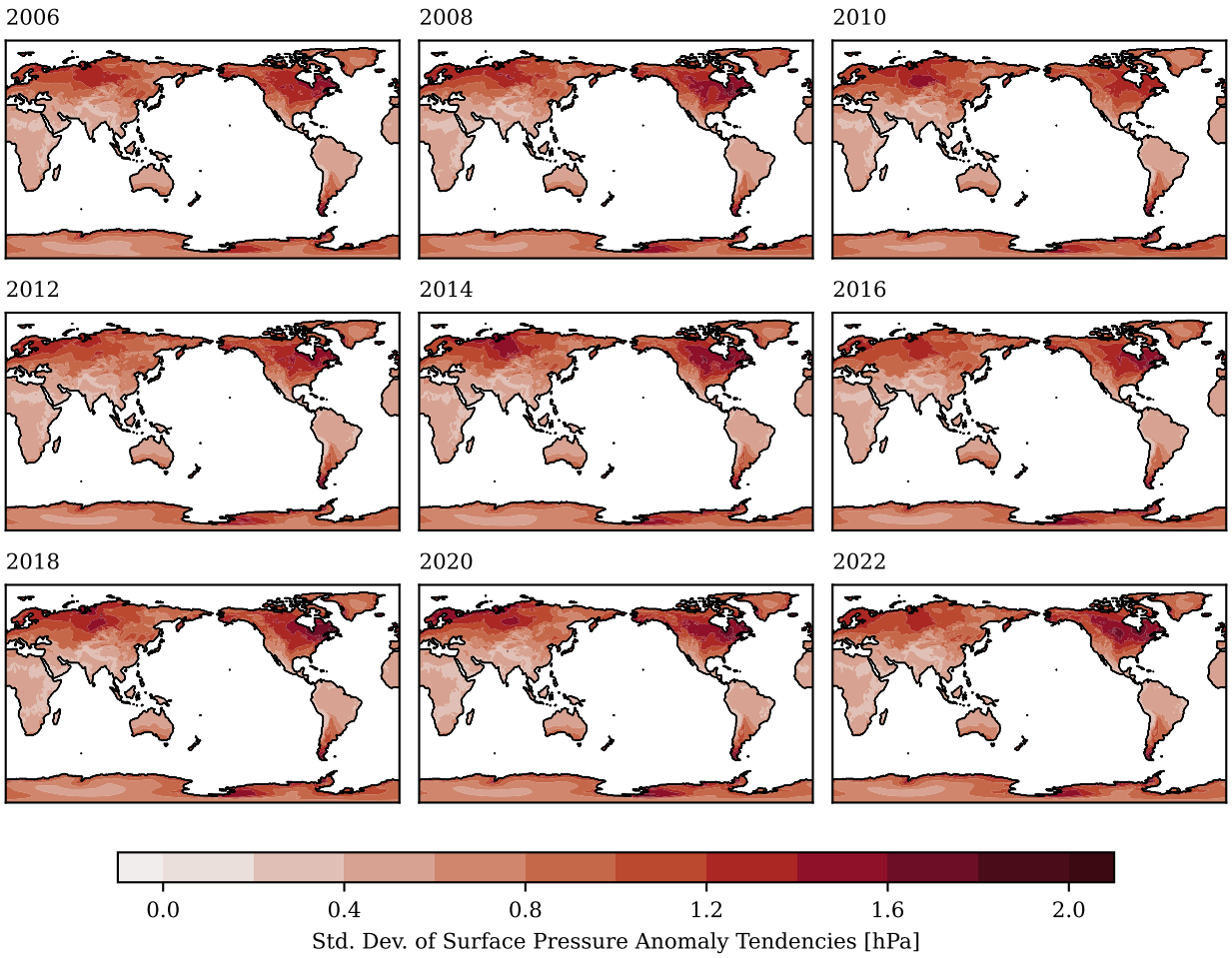

Figure 2.5: Standard deviation of 3 hourly tendencies of atmospheric surface pressure as included in AOD1B RL07.

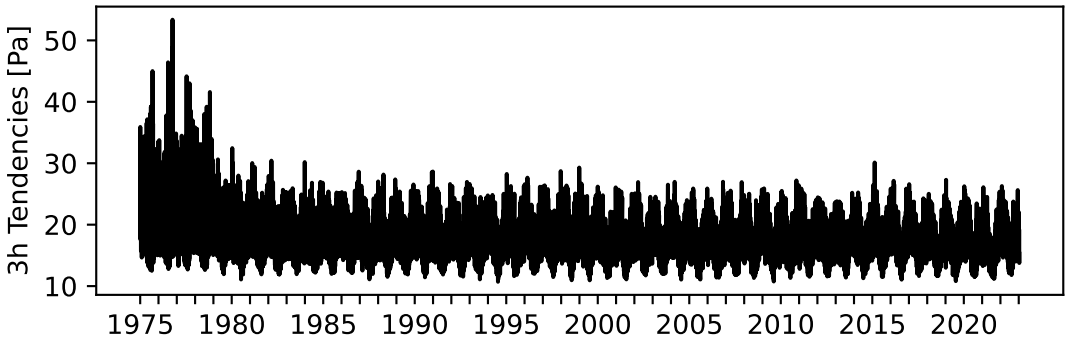

Figure 2.6: Area-weighted global mean of absolute values of 3 hourly tendencies of atmospheric surface pressure as included in AOD1B RL07.

Chapter 3

Dynamic Ocean Contribution to Bottom Pressure Variability

3.1 OGCM Configuration

The ocean component of AOD1B is based on a numerical simulation with the Max-Planck-Institute for Meteorology Ocean Model (MPIOM; Jungclaus *et al.*, 2013). It is a general ocean circulation code discretized globally on an Arakawa C-grid in the horizontal, and a z-grid in the vertical. It includes a sea-ice module (Notz *et al.*, 2013) that utilizes the viscous-plastic rheology of Hibler (1979).

Decades-long numerical model development efforts by Ernst Maier-Reimer (1944 – 2013; Hasselmann, 2013) and his colleagues in Hamburg resulted in a series of high-quality software packages, as, e.g., the Large-Scale Geostrophic Ocean General Circulation Model (LSG; Maier-Reimer & Mikolajewicz, 1992), the Hamburg Ocean Primitive Equation Model HOPE (Drijfhout *et al.*, 1996; Wolff *et al.*, 1997), and the first release of MPIOM (Marsland *et al.*, 2003). We are using revision 3932 with a number of changes.

A few changes have been performed to the code in order to make use of experience gained with previous releases during the most recent years in the context of simulating ocean bottom pressure variability, which in particular includes the activation of atmospheric surface pressure forcing. Additionally, we have implemented the full feedbacks from the effects of Self-Attraction and Loading (SAL) into the momentum equations as described in Shihora *et al.* (2022b). The SAL feedback not only includes the contribution from ocean bottom pressure anomalies but also includes the impact of atmospheric surface pressure anomalies over the continents. A medium-resolution configuration of MPIOM is used here that is discretized on a 1.0° tri-polar grid with 40 vertical layers (TP10L40). The internal time-step of the model is 20 min, and ocean state quantities and associated diagnostics as ocean bottom pressure and horizontal currents necessary to derive ocean angular momentum changes relevant for Earth rotation research (Dobslaw *et al.*, 2010) are stored every 3 hours.

3.2 Atmospheric Forcing Data

Dynamics simulated by MPIOM in our particular model experiment are driven by atmospheric forcing only, and no observational constraints are introduced into the simulation by means of data assimilation. As for previous releases of AOD1B, luni-solar gravitational tides in the oceans are not simulated, but tidal waves in response to periodically varying atmospheric pressure loading and

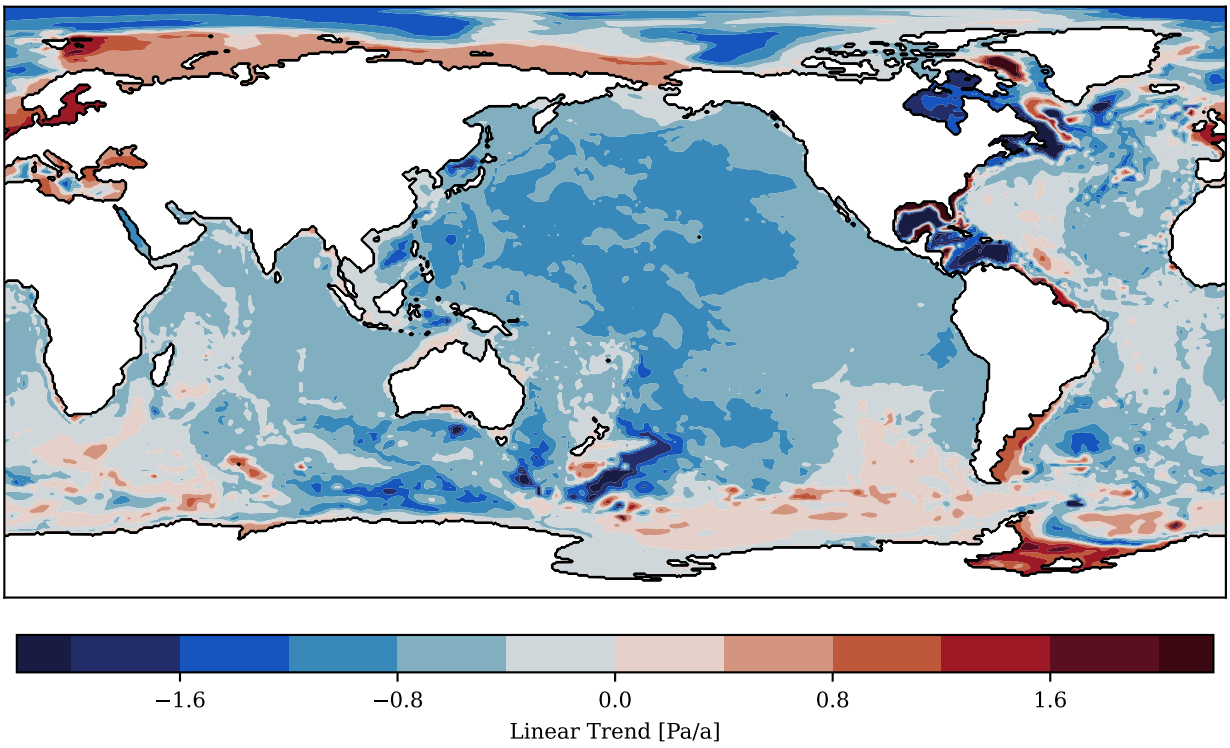

Figure 3.1: Trend in the dynamic ocean contribution to bottom pressure obtained from the last 50 years of the 2000 year long MPIOM spin-up simulation.

surface winds are part of the simulated ocean bottom pressure field. Those signals are separated during post-processing from the non-tidal AOD1B coefficients as discussed in Ch. 5.

The simulation is initialized from 3D temperature and salinity climatologies (Levitus, 2005) followed by a spin-up simulation under cyclic atmospheric forcing conditions with daily sampling as prepared for an ocean model intercomparison project (Röske, 2005). The spin-up simulation has been integrated over 2000 years, remaining trends in ocean bottom pressure are less than ±2 Pa a^{-1} on regional scales, and ±4 Pa a^{-1} even for individual grid points (Fig. 3.1). The spin-up is followed by a transient simulation with hourly atmospheric forcing obtained from ERA5 for the period 1960 – 2017 and from the operational ECMWF data for all subsequent years.

MPIOM requires the following atmospheric forcing data-sets: atmospheric surface pressure; horizontal surface wind stress, surface wind speed, temperature and dew point temperature at 2 m above the surface; cloud cover, short-wave incoming radiation at the surface, precipitation, 10m wind speed as well as horizontal wind stress components.

3.3 Post-Processing of Simulated Bottom Pressure

Ocean bottom pressure is a standard output variable of MPIOM that hydrostatically sums the contributions of air and water masses along the plumb line. For the separation of the oceanic contribution to bottom pressure, the atmospheric surface pressure applied as a forcing data-set is subtracted. In order to remove artificial fluctuations in total ocean mass induced by the Boussinesq approximation employed in the MPIOM momentum equations, the mean bottom pressure averaged over the whole ocean domain is removed by subtracting a homogeneous shell of mass at every time-step (Greatbatch, 1994):

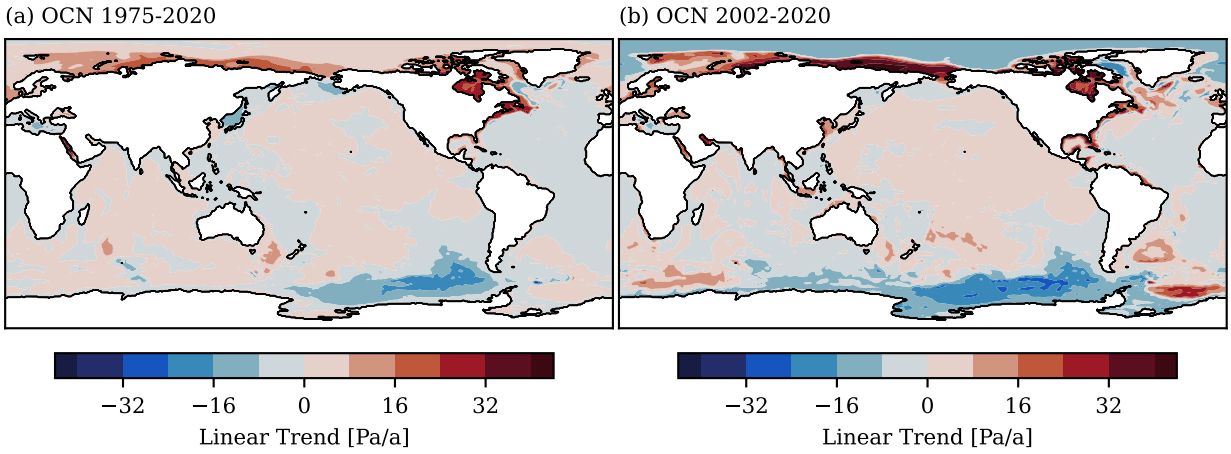

Figure 3.2: Trend in the dynamic bottom pressure over the period 1975 – 2020 (left) and 2002 – 2020 (right) as included in AOD1B.

$$p_b'(\theta,\phi) = p_b(\theta,\phi) - \frac{1}{A_{\text{Oceans}}} \iint_{\text{Oceans}} p_b(\theta,\phi) dA \tag{3.1}$$

Subsequently, tidal fluctuations as discussed in Ch. 5 are estimated and removed, and the long-term mean ocean bottom pressure averaged over the period 2007 – 2014 is subtracted to arrive at pressure anomalies.

In the following, we will exclusively discuss bottom pressure anomalies that exclude the static contribution of the mean atmospheric surface pressure in all oceanic regions, which is called "dynamic contribution to bottom pressure" or "dynamic bottom pressure" in the remainder of this document. Pressure anomalies are transformed into Stokes coefficients up to d/o 180 as described in Sect. 2.5 by assuming that all mass variability takes place at the surface of the reference ellipsoid, which implies that both ξ and h are assumed to be zero over the oceans.

3.4 Spatial Patterns of Trends and Variabilities

Stokes coefficients of the dynamic ocean contribution to the time variations of the Earth's gravity field are resynthesized back onto an equi-angular grid for a series of consistency checks as reported below. Long-term trends obtained from the years 1975 – 2020 are in the range of 15 Pa a^{-1} regionally. They mostly take place in the surroundings of the ACC and therefore reflect adjustment of the ocean dynamics to the ECMWF-based wind forcing. Trend patterns are, however, largely different when compared to the trends obtained from the spin-up run, thereby indicating that the remaining trends are not related to ongoing deep-sea adjustment processes or artificial drift in the model. In addition, trends are only slightly larger than corresponding atmospheric trends, which is an acceptable level of accuracy in view of the currently available length of the satellite gravimetry data record.

Yearly means of ocean bottom pressure reveal signals of a few hPa in particular in the Southern Ocean (Fig. 3.3) that are primarily related to large-scale changes in surface winds and thus time-varying transports in the Antarctic Circumpolar Current (Bergmann & Dobslaw, 2012). Signals of comparable magnitude are also present in the Arctic Ocean, whereas low frequency variability in all other oceanic regions apart from the semi-enclosed seas are much smaller.

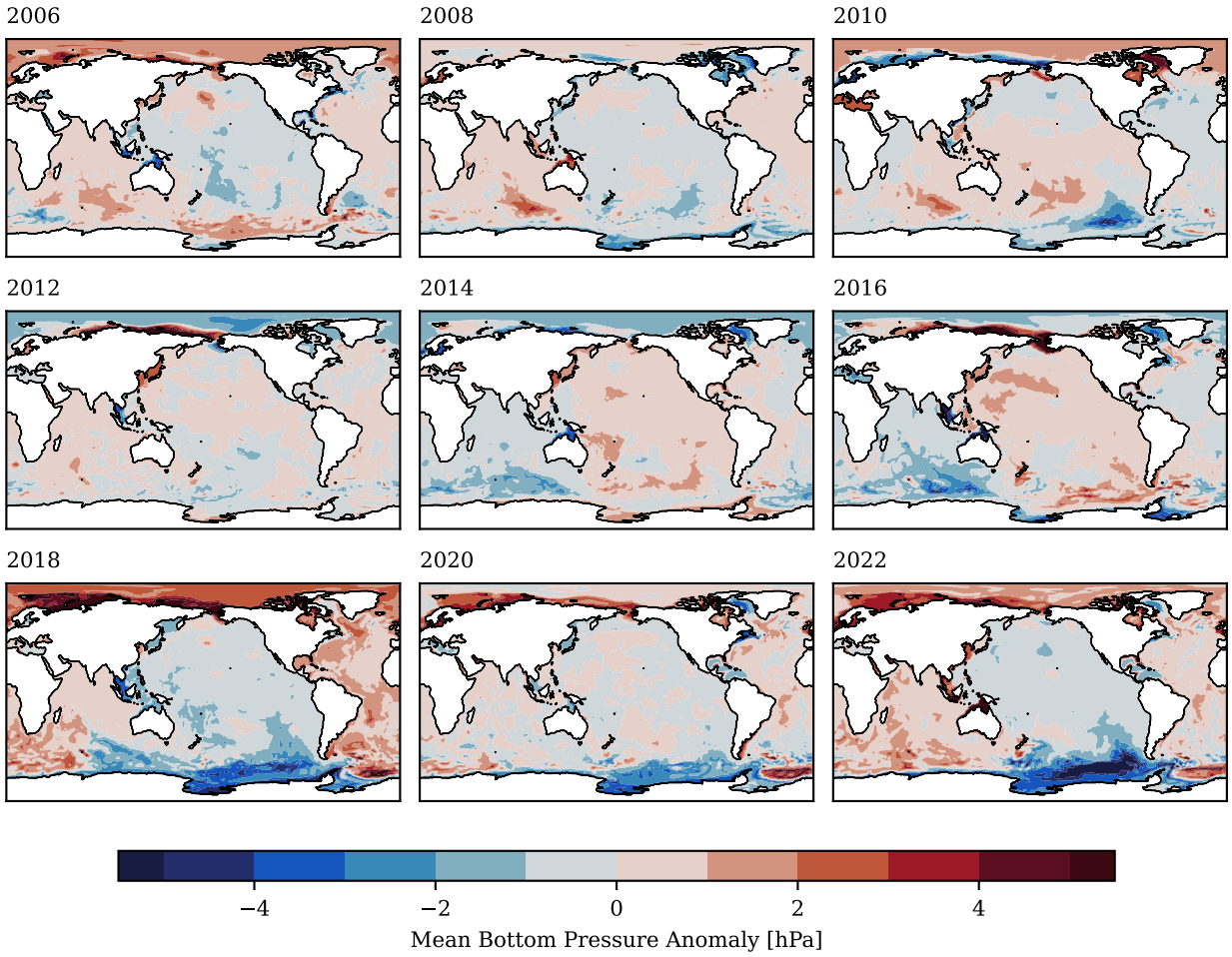

Figure 3.3: Yearly means of dynamic ocean bottom pressure for the years 2006 – 2022 as included in AOD1B.

Variability in simulated dynamic ocean bottom pressure is fairly consistent throughout the years thanks to the consistency in the atmospheric forcing data sets (Fig. 3.4). Strongest variability takes place close to the coasts and within semi-enclosed seas as the North Sea or within the Indonesian Archipelago, whereas open-ocean signals are strongest in the surroundings of the Antarctic Circumpolar Current.

3.5 Assessment of 3-Hourly Tendencies

We also calculate differences of consecutive 3-hourly time-steps of the re-synthesized anomalies in the gravity potential expressed in terms of equivalent bottom pressure (Figs. 3.5 & 3.6). Those tendencies will be particularly large at times where a jump in the series appears. Several notable features are found, especially in the time-series of spatially averaged tendencies. First, there is an overall increase in the oceanic variability in the earlier years which is associated with the higher variability in atmospheric surface pressure in the ERA5 re-analysis back-extension as described in Ch. 2. Secondly, there is a slight decrease in the tendencies with the introduction of the operational ECMWF atmospheric data in the beginning of 2018. This can be attributed to the change in tempral resolution of the atmospheric forcing data in MPIOM. Whereas the ERA5 reanalysis data is used with an hourly resolution, the operational forecast data uses 3-hourly forcing. As a result,

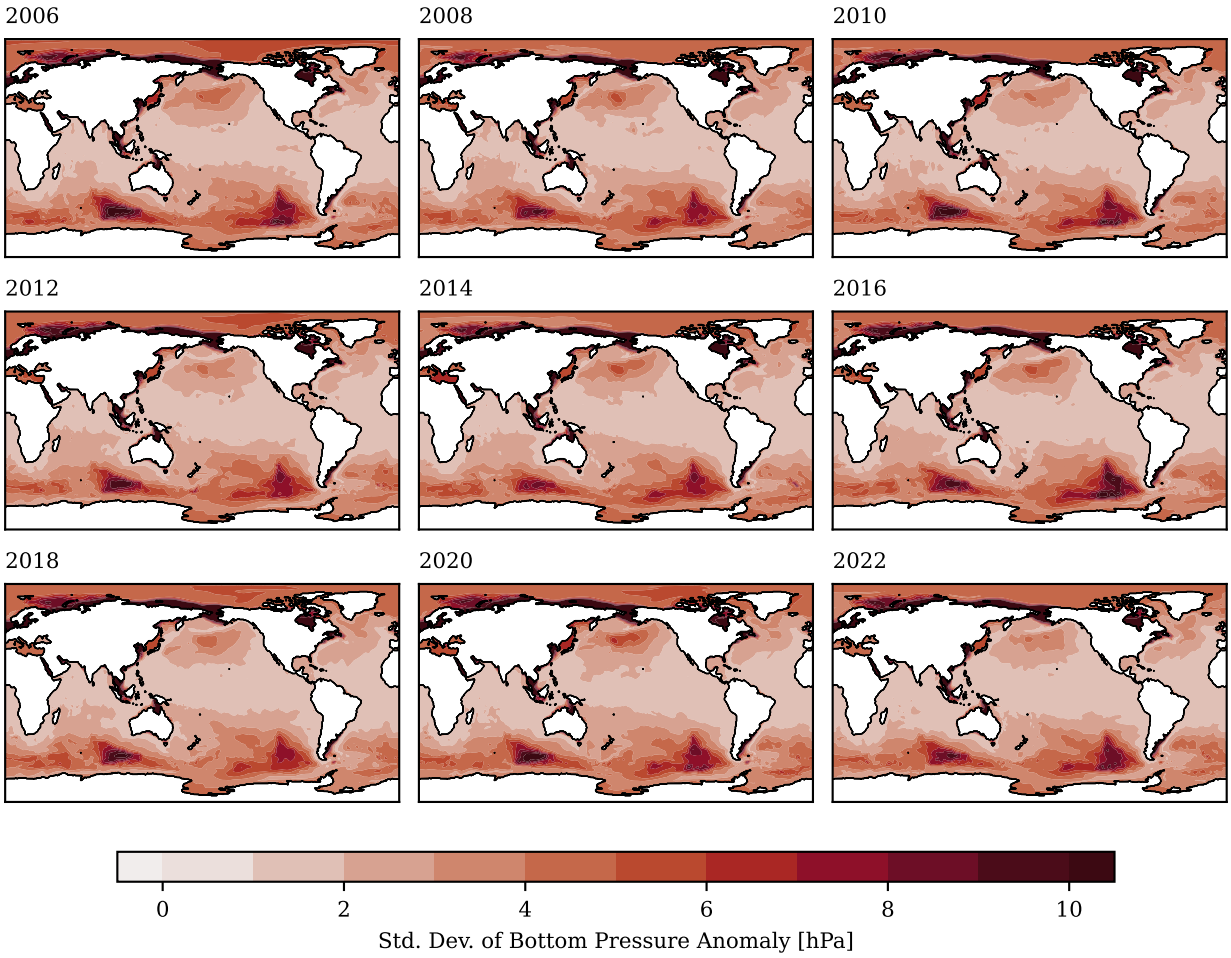

Figure 3.4: Standard deviation of variability of 3 hourly dynamic ocean bottom pressure anomalies as included in AOD1B RL07 calculated individually for the years 2006 – 2022.

advected atmospheric fronts are less sharply defined and thus lead to a reduction in the variability. Additional assessments of the transition can be found in Shihora *et al.* (2023b). Lastly, small peaks are visible in the tendency time-series. These appear both under ERA5 and operational forecast forcing data and are similarly present in AOD1B RL06 at the same times. Further analysis (Shihora *et al.*, 2023b) shows that these are related to resonances in oceanic basins at semi-diurnal time-scales.

While there are notable features in the tendency time-series, they can be readily explained and do not degrade the quality of AOD1B RL07. There is no evidence for technical inconsistencies.

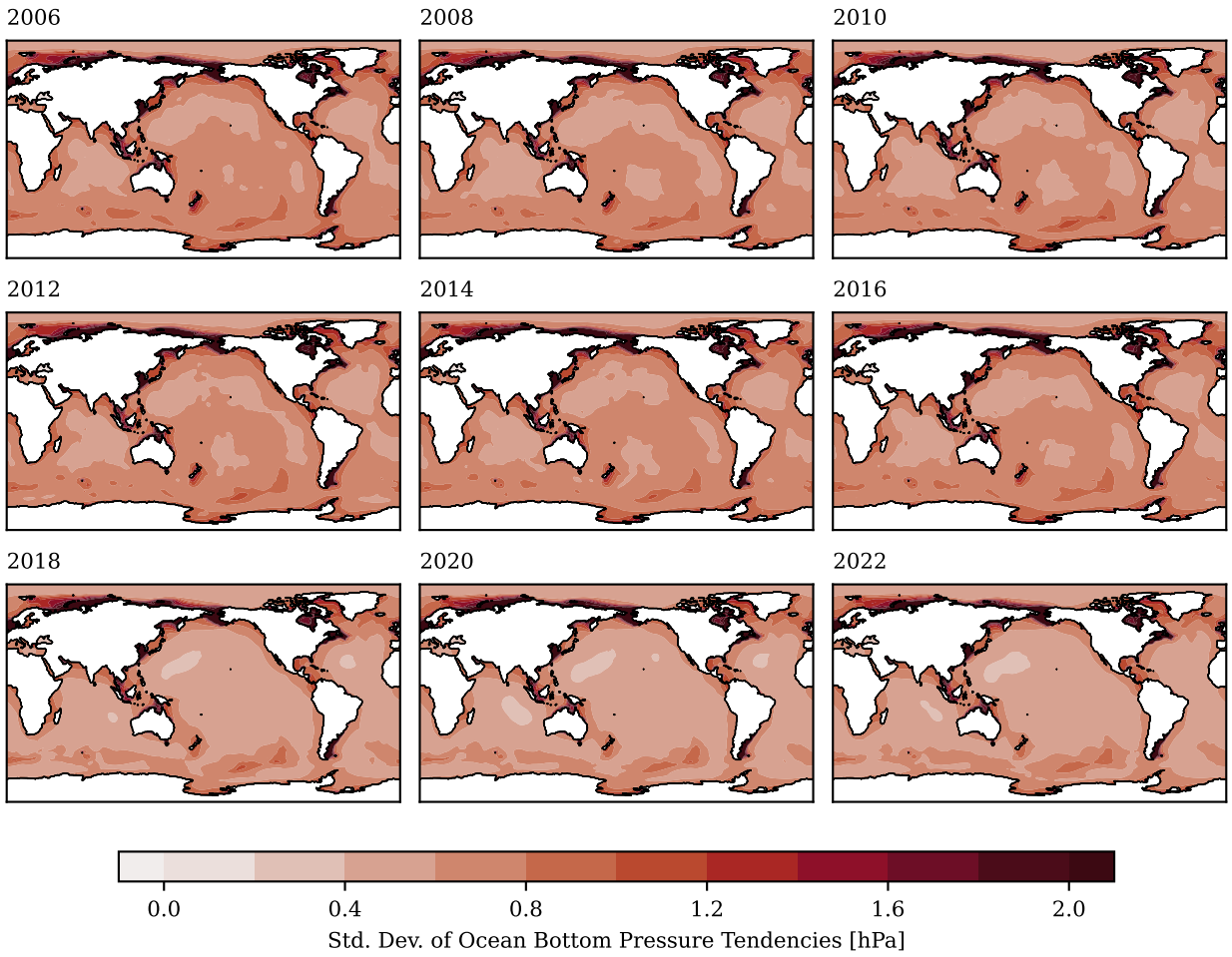

Figure 3.5: Standard deviation of 3 hourly tendencies of dynamic ocean bottom pressure as included in AOD1B RL07.

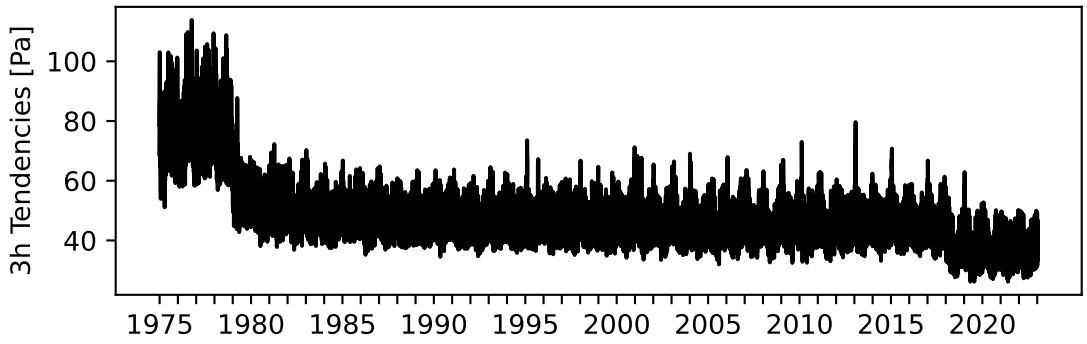

Figure 3.6: Area-weighted global mean of absolute values of 3 hourly tendencies of dynamic ocean bottom pressure as included in AOD1B RL07.

Chapter 4

Attraction Effects of Upper-Air Density Anomalies

4.1 Atmospheric Density Data at Sigma Model Levels

Current state-of-the-art numerical weather prediction (NWP) models are sometimes discretized in the vertical at hybrid sigma levels, that smoothly follow the orography and are thus able to represent troposphere dynamics over rugged terrain more realistically. At higher altitudes, however, hybrid levels tend to align to the isobaric surfaces. Both the current IFS cycle (48r1) as well as the ERA5 reanalysis employ $k = 137$ levels. The topmost level with a pressure of typically 1 Pa is indicated by k=1, whereas $k = k_{\max} + 1/2$ corresponds to the surface orography as the lower boundary of the atmosphere. Atmospheric pressure at the interface (i.e., half-level) between two levels is obtained from surface pressure p_s and the coefficients $a_{k+1/2}$ and $b_{k+1/2}$ that define the vertical grid:

$$p_{k+1/2} = a_{k+1/2} + b_{k+1/2}\, p_s \tag{4.1}$$

Atmospheric density at full levels is conveniently represented by the virtual temperature T_v that can be derived from 3D temperature T and specific humidity q by incorporating the gas constants for both dry air R_d and water vapour R_v:

$$T_v = T\left(1 + \frac{1 - \dfrac{R_d}{R_v}}{\dfrac{R_d}{R_v}}\, q\right) \tag{4.2}$$

$$\approx T(1 + 0.608\, q) \tag{4.3}$$

The virtual temperatures are subsequently integrated vertically upwards to obtain the geopotential Φ at the level interfaces by starting from the surface geopotential at $k = k_{\max+1/2}$ with

$$\Phi_{k-1/2} = \Phi_{k+1/2} + \frac{R_d}{g_{\mathrm{WMO}}} T_{vk} \ln\left(\frac{p_{k+1/2}}{p_{k-1/2}}\right) \tag{4.4}$$

The geopotential heights $H_k = \Phi_k / g_{\mathrm{WMO}}$ at full model level k that represent the height of the pressure element $\Delta p_k = p_{k+1/2} - p_{k-1/2}$ are finally transformed into orthometric heights by utilizing eq. 2.11.

Finally, the full atmospheric mass distribution discretized at the model levels k forms the inner integral of eq. 2.7 as follows:

$$\Delta I_l = \int_0^{\infty} \left(\frac{r}{a_{45}}\right)^{l+2} \rho(r) dr \tag{4.5}$$

$$= \sum_{k=1}^{k_{\max}} \left(\frac{a + z_k}{a_{45}}\right)^{l+2} \frac{\Delta p_k}{g} \tag{4.6}$$

4.2 Separation of Upper-Air Density Attraction Effects

The inner integral of the 3D atmospheric masses as given in eq. 4.6 does include the summarized effect of both surface pressure and the contributions of density anomalies above ground. For AOD1B, we subtract the effect of surface pressure which has been already treated in Ch. 2:

$$\Delta I_l = \left[\sum_{k=1}^{k_{\max}} \left(\frac{a + z_k}{a_{45}}\right)^{l+2} \frac{\Delta p_k}{g}\right] - \left(\frac{a + z_{\mathrm{mdp}}}{a_{45}}\right)^{l+2} \frac{p_s}{g} \tag{4.7}$$

where the orthometric height of the mass mid-point of the air column z_{mdp} is approximated from the surface geopotential of a reference atmospheric density profile. The inner integral of residual atmospheric masses that cause an additional attraction effect on the Earth's gravity field are subsequently analysed into spherical harmonics with eq. 2.14. Note that k_l' is set to zero in this case, since upper-air mass anomalies do not cause a deformation of the Earth's surface.

4.3 Spatial Patterns of Trends and Variabilities

Stokes coefficients of the attraction effect of upper-air density anomalies to the time-variations of the Earth's gravity field are synthesized back onto an equi-angular grid for a series of consistency assessments as reported below. Re-synthesis has been again performed with eq. 2.23 to allow for an easy cross-comparison with the effects of atmospheric surface pressure and ocean bottom pressure.

Secular trends in the effects of upper-air density anomalies on the Earth's gravity field are computed over the period 1975 – 2020 (Fig. 4.1 a) and 2002 – 2020 (Fig. 4.1 b) in terms of equivalent surface pressure changes. The trends only amount to about 0.25 Pa a^{-1} when estimating from 2002 – 2020 and even less over longer periods. These are perceived to fit well into the range of natural climate variability and therefore does not introduce artificial drift into AOD1B.

Annual mean signals (Fig. 4.2) are in the range of 10 Pa and thus by a factor of 50 smaller than the contributions of atmospheric surface pressure.

Similarly, the yearly standard deviation (Fig. 4.3) is homogeneous over the years considered. Signal variability is concentrated in the regions where the sub-polar jets show large intra-seasonal variability and thus cause anomalies in the upper-air density fields. However, variability is again much smaller than the corresponding effect of the atmospheric surface pressure discussed in Ch. 2.

4.4 Assessment of 3-Hourly Tendencies

We also calculate differences of consecutive 3-hourly time-steps of the re-synthesized anomalies in the gravity potential caused by upper-air density anomalies expressed in terms of equivalent surface

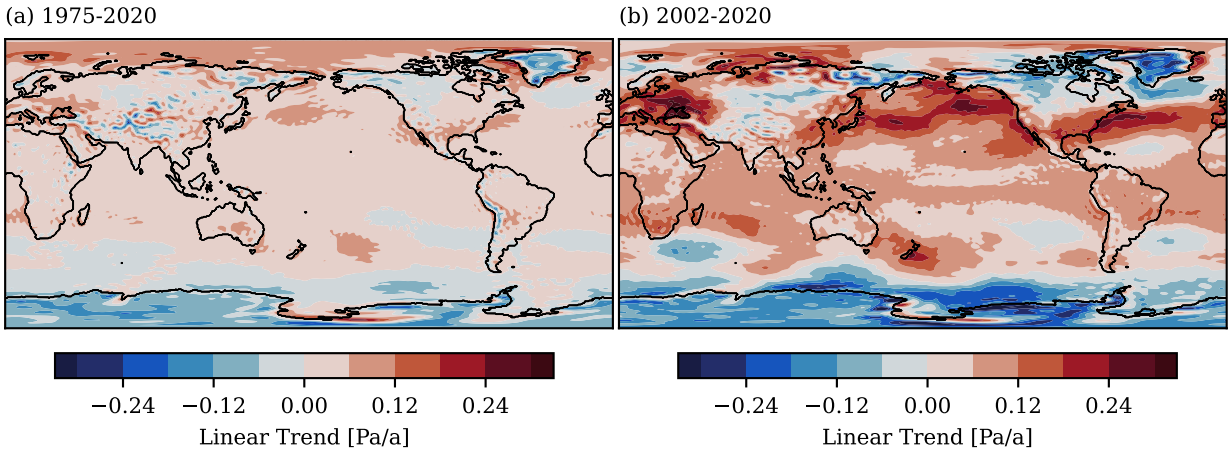

Figure 4.1: Trend in the effect of upper-air density anomalies on the Earth's gravity field as included in AOD1B over the period 1975 – 2020 (a) and 2002 – 2020 (b) as expressed in equivalent surface pressure changes at the reference orography.

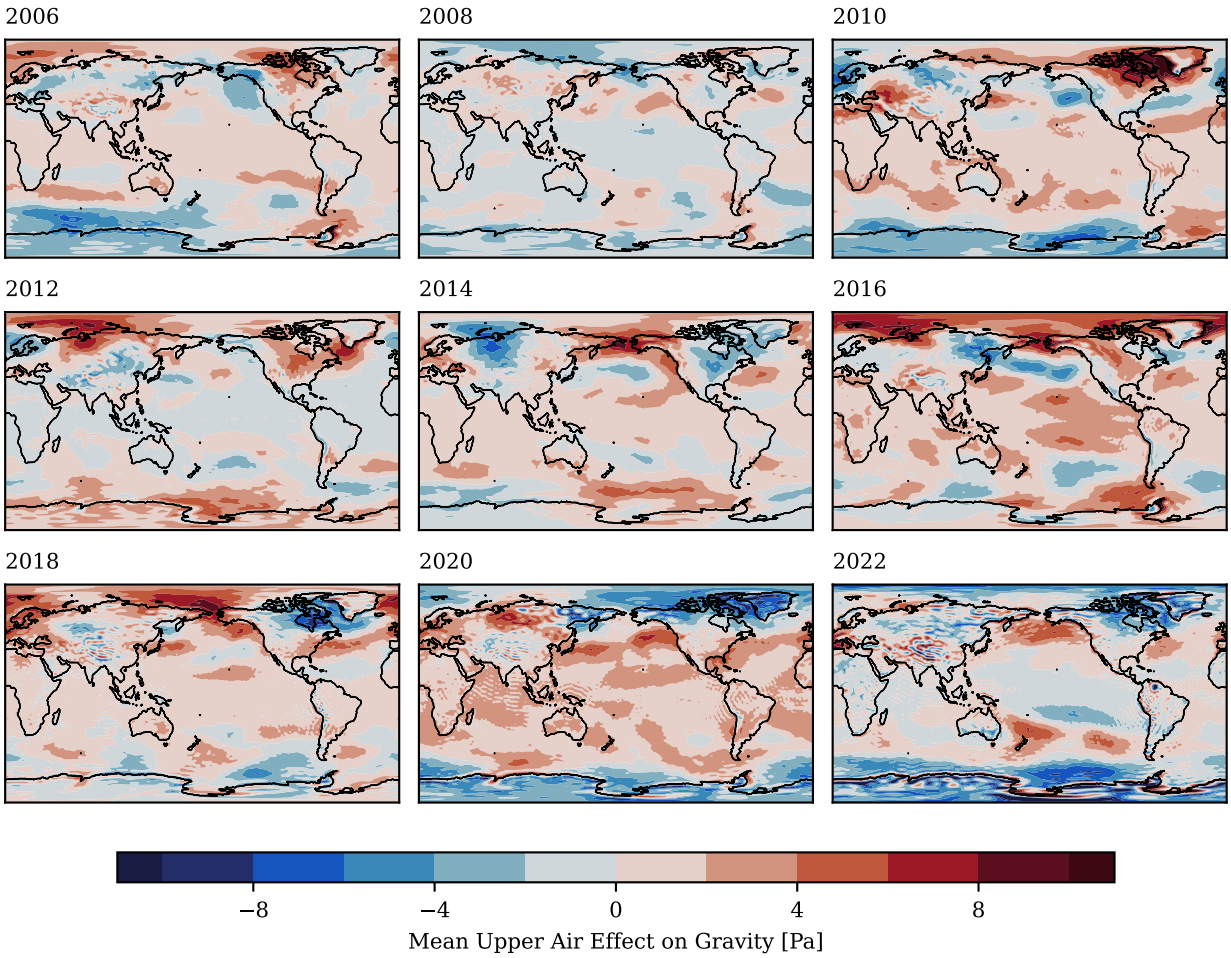

Figure 4.2: Yearly means in the effect of upper-air density anomalies on the Earth's gravity field as included in AOD1B for the period 2006 – 2022 as expressed in equivalent surface pressure changes.

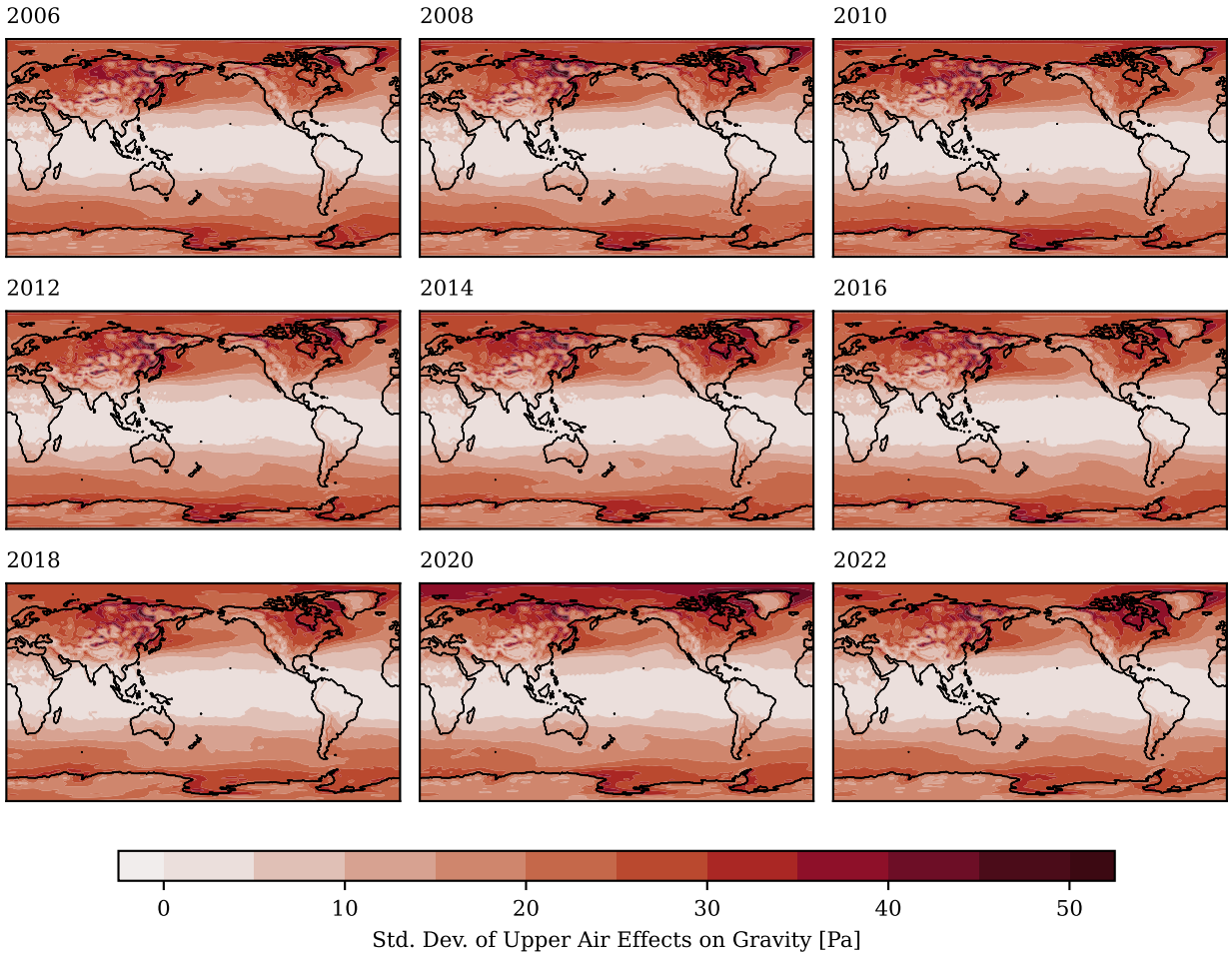

Figure 4.3: Standard deviation of 3 hourly effect of upper-air density anomalies on the Earth's gravity field as included in AOD1B calculated individually for the years 2006 – 2022 as expressed in equivalent surface pressure changes.

pressure. Those tendencies will be particularly large at times where a jump in the series appears. However, neither the yearly standard deviations of the tendencies (Fig. 4.4) nor the time-series of area-averaged absolute values of the tendencies (Fig. 4.5) give evidence for such inconsistencies. We note, however, a decrease of the average global tendencies at the beginning of the year 2018 which is related to the higher spatial resolution of the operational ECMWF data. In addition, the impact of the ERA5 back-extension data can be seen here as well for the earliest years of AOD1B (1975 – 1978). In view of the dominance of the atmospheric surface pressure contribution to changes in the Earth's gravity field, however, we conclude that this feature does not significantly affect the consistency of AOD1B in view of its intended applications in satellite gravimetry.

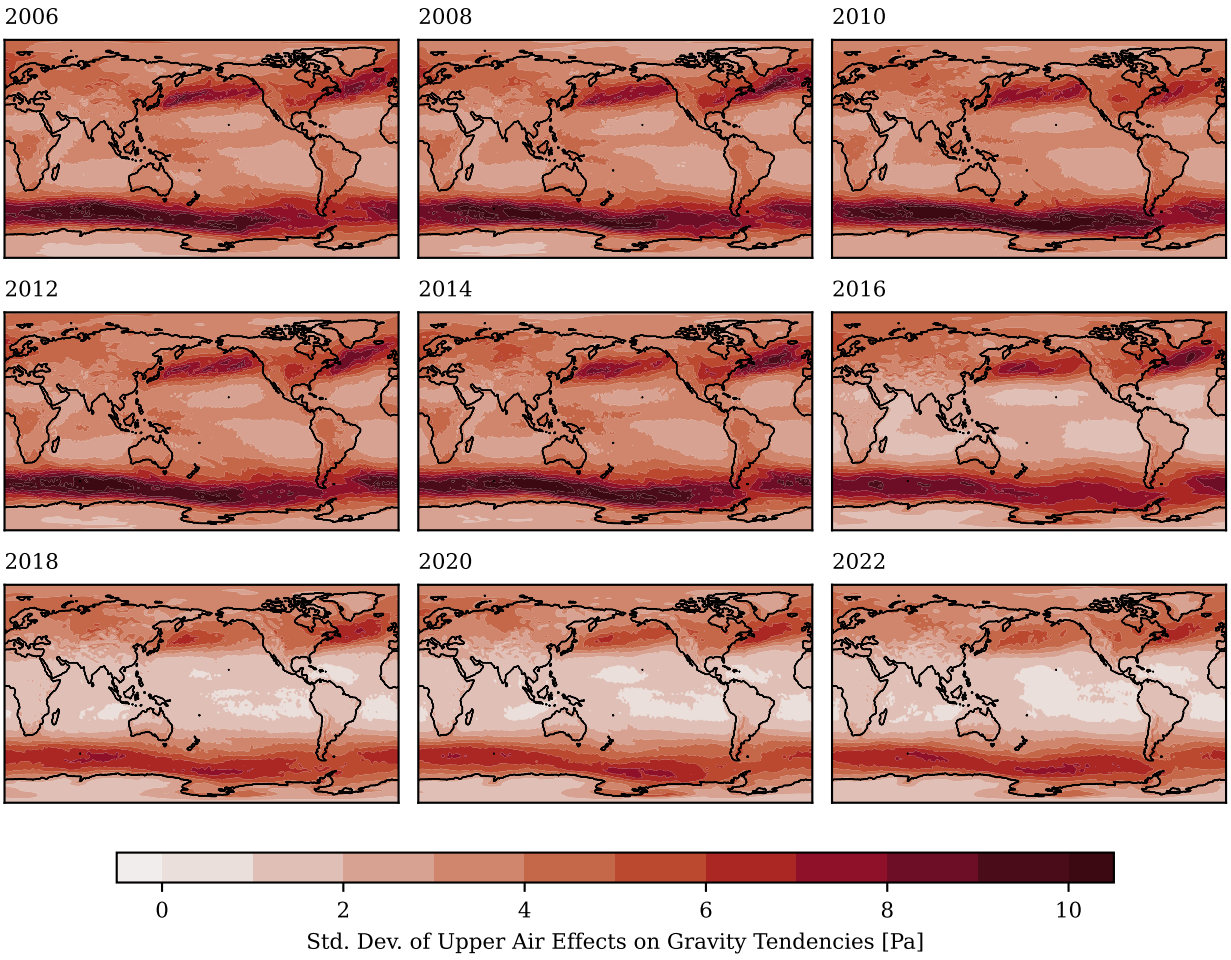

Figure 4.4: Standard deviation of 3 hourly tendencies of upper air density anomalies as included in AOD1B RL07.

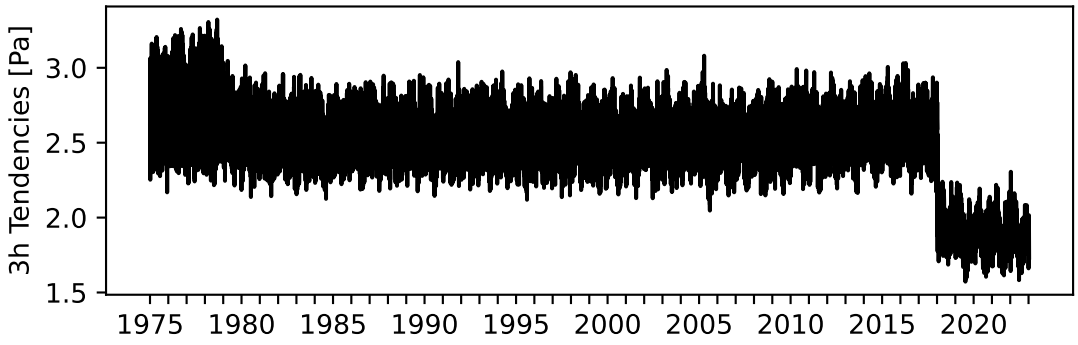

Figure 4.5: Area-weighted global mean of absolute values of 3-hourly tendencies of upper air density anomalies as included in AOD1B RL07.

Chapter 5

Removal of Atmospheric Tides

5.1 Atmospheric Tides in ECMWF Surface Pressure

Atmospheric tides are to be understood here as periodic variations of atmospheric pressure relative to the moving surface of the Earth, which is the Earth's crustal surface in continental regions, and the ocean surface elsewhere. These tides are conventionally observed by pressure gauges attached to the ground, or tied to floating objects as buoys or ships.

Tides in the atmosphere are excited by two different mechanisms that are principally known already for decades: First, absorption of solar radiation by both water vapour (IR) and ozone (UV) creates large periodic temperature variations in the middle atmosphere that propagate vertically as approximately described by the thermal wind equations and cause large-scale variations in atmospheric surface pressure. The frequencies of this process are fundamentally governed by the incidence angle of solar radiation, so that periods of 24 hours and overtones may occur. Signals are not strictly periodic but vary in amplitude due to variations in solar insolation; changes in the atmospheric density of the lower troposphere affecting vertical wave propagation; and transient convective processes near the surface that cause periodic pressure variations at periods of 24 hours as well.

Secondly, tidal waves in the atmosphere are excited by direct gravitational attraction of atmospheric masses by the tide-generating bodies Sun and Moon, and – more importantly – also by periodic motions of the lower boundary of the atmosphere caused by both tides in the solid Earth and in the oceans. For this process, also secondary gravitational effects due to the modified mass distribution caused by ocean and solid Earth tides add small modifications to the signals.

The representation of surface atmospheric tides in global atmospheric model data has been validated in many aspects with the help of thoroughly screened sets of globally distributed in situ pressure gauges. Those analyses indicate that the principal frequencies S_1 and S_2 are quite well represented by ECMWF, even though a "small but probably significant overestimation of up to 18% for peak semidiurnal amplitudes" is reported (Schindelegger & Ray, 2014).

Based on a thorough pre-assessment of the tidal signals in the ECMWF data-set to be used for AOD1B, we selected the following strategy to cope with atmospheric tides in AOD1B RL07 based on the work of Balidakis *et al.* (2022):

- In total, harmonic amplitudes of 16 tidal frequencies are estimated and removed from the ECMWF surface pressure. This includes the main solar tides S_1, S_2, and S_3 as well as the main semidiurnal lunar tide M_2. Due to the higher hourly resolution of the ERA5 data, higher frequency constituents up to the S_6 are considered as well.

Table 5.1: Extended Doodson (solar-day-based) and Delaunay argument multipliers (Hartmann & Wenzel, 1995; Simon, 2013) for 16 waves of diurnal and shorter periods in atmosphere and ocean that are estimated and removed from AOD1B RL07.

Darwin name	Frequency [° h^{-1}]	Doodson arguments							Delaunay arguments						Argument at J2000 [°]
		τ	s	h	p	N'	p_s	90°	γ	l	l'	F	D	Ω	
π_1	14.91786609	1	1	-3	0	0	1	-1	1	0	1	2	-2	2	171.999
P_1	14.95893277	1	1	-2	0	0	0	-1	1	0	0	2	-2	2	169.528
S_1	15.00000141	1	1	-1	0	0	1	1	1	0	1	0	0	0	192.932
K_1	15.04107005	1	1	0	0	0	0	1	1	0	0	0	0	0	190.461
ψ_1	15.08213673	1	1	1	0	0	-1	1	1	0	-1	0	0	0	187.990
M_2	28.98410705	2	0	0	0	0	0	0	2	0	0	2	0	2	124.288
T_2	29.95893614	2	2	-3	0	0	1	0	2	0	1	2	-2	2	2.459
S_2	30.00000282	2	2	-2	0	0	0	-1	2	0	0	2	-2	2	269.988
R_2	30.04106950	2	2	-1	0	0	-1	2	2	0	-1	2	-2	2	177.517
K_2	30.08214010	2	2	0	0	0	0	0	2	0	0	0	0	0	200.921
T_3	44.95893559	3	3	-4	0	0	0	0	3	0	0	4	-4	4	259.516
S_3	45.00000423	3	3	-3	0	0	0	2	3	0	0	3	-3	3	359.983
R_3	45.04107287	3	3	-2	0	0	0	0	3	0	0	2	-2	2	100.449
S_4	60.00000564	4	4	-4	0	0	0	0	4	0	0	4	-4	4	359.977
S_5	75.00000705	5	5	-5	0	0	0	0	5	0	0	5	-5	5	179.971
S_6	90.00000846	6	6	-6	0	0	0	0	6	0	0	6	-6	6	359.965

- Since interannual variations in atmospheric tides have been found to be less reliable in older years (Balidakis *et al.*, 2023), tidal signals at the 16 selected frequencies have been estimated and removed for each year separately before 2018.
- Following 2018 and the use of operational ECMWF data with a 3-hourly resolution, all tidal signals up to the S_3 are considered. Those signals are estimated once over the period of 2018 – 2020, and are subsequently subtracted from all later years as well.

5.2 Removed Tidal Signals From Atmospheric Surface Pressure

In total, 16 frequencies are considered to be relevant for the removal of atmospheric tides. Here, we employ standard oceanographic naming conventions introduced by Arthur Thomas Doodson, which consequently implies to label the main semi-diurnal lunar tide as M_2. Note that in the meteorologic or aeronomic literature, this frequency is often labelled as L_2. For the naming conventions of S_3 modulations, we follow the suggestions by Ray & Poulose (2005), phase conventions applied for S_1 are consistent with Ray & Egbert (2004). The tidal arguments applied are given in Tab. 5.1.

For the tidal analysis, sine and cosine components for each frequency are estimated from a least-squares fit (Fig. 5.1) for each year of atmospheric surface pressure anomalies. Tidal signals of S_1 and S_2 exceed 1 hPa in many regions and are largely consistent with previous knowledge on atmospheric tides both based on alternative numerical weather models and in situ observation compilations (Fig. 5.1). Signals for both S_3 and M_2 are substantially smaller and reach amplitudes of about 10 Pa only. Similar amplitudes are also obtained for the side-bands as well as constituents of higher frequency.

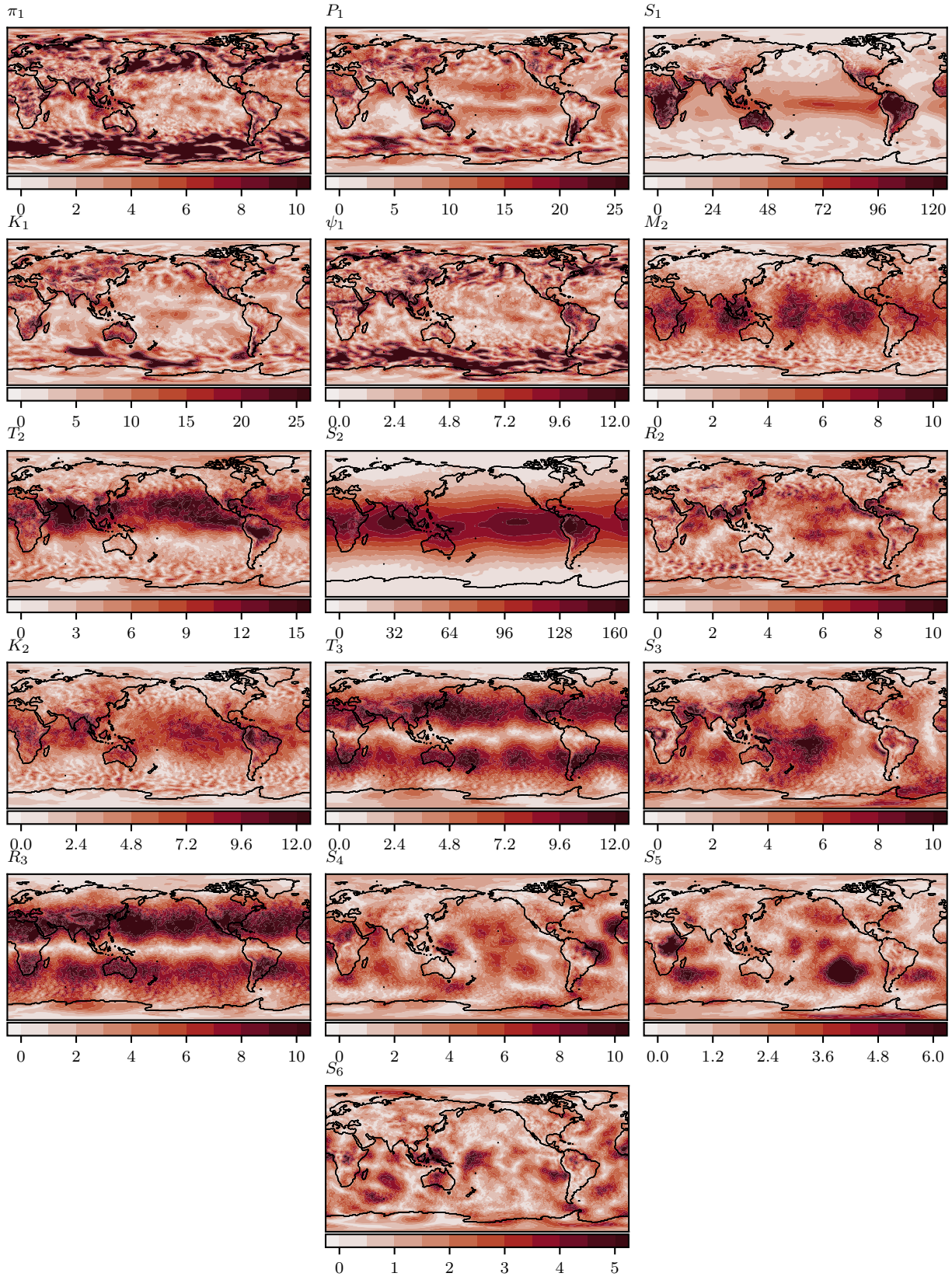

Figure 5.1: Exemplary surface pressure harmonic amplitudes of atmospheric tides [Pa] for the tidal constituents removed from AOD1B RL07 as estimated over the year 2014.

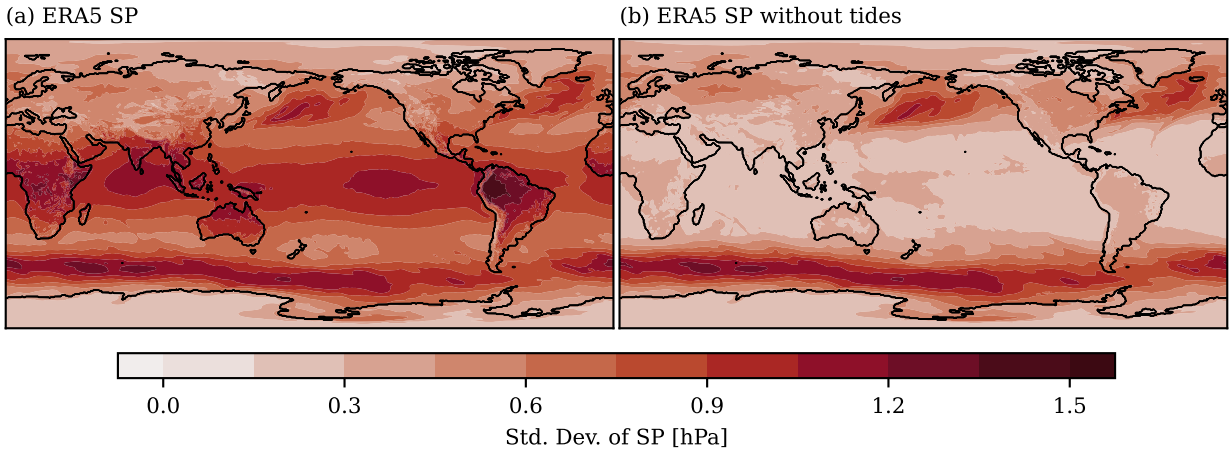

Figure 5.2: Sub-daily variability of ERA5 surface pressure including tidal signals (a) or after their removal (b).

To test the efficacy of our selected approach to estimate and remove tides, we show the reduction in sub-daily surface pressure standard deviation in Fig. 5.2.

For atmospheric surface pressure, tidal signals are very prominent at tropical latitudes and the variability is drastically reduced at those latitudes. In mid-latitude regions, however, almost none of the sub-daily variability is explained by atmospheric tides. Please note that some tracks of major tropical storms are now visible in Fig. 5.2 thanks to the otherwise strongly reduced variability.

5.3 Tidal Signals in Upper-Air Density Anomalies

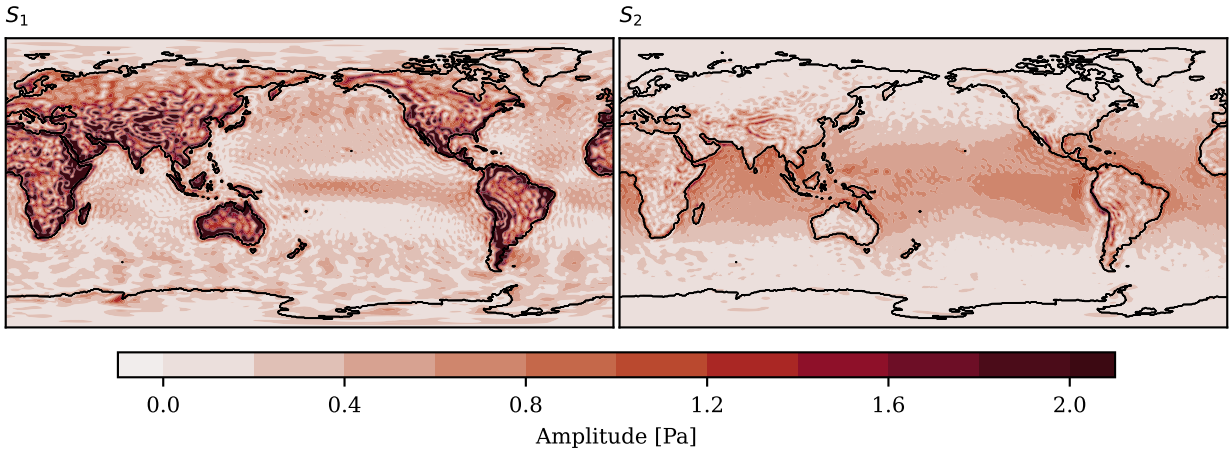

Figure 5.3: Exemplary S_1 and S_2 tidal signals in the upper air density anomalies [Pa] as estimated over the year 2014.

For completeness, we also test for the presence of tidal signals in the contributions of upper-air density anomalies to changes in the Earth's gravity field (Figs. 5.3 & 5.4) as introduced in Ch. 4. Tidal signals in the re-synthesized coefficients expressed in equivalent surface pressure anomalies are always well below 2 Pa, thereby confirming that tidal variability of upper-air density can be safely neglected for satellite gravimetry applications.

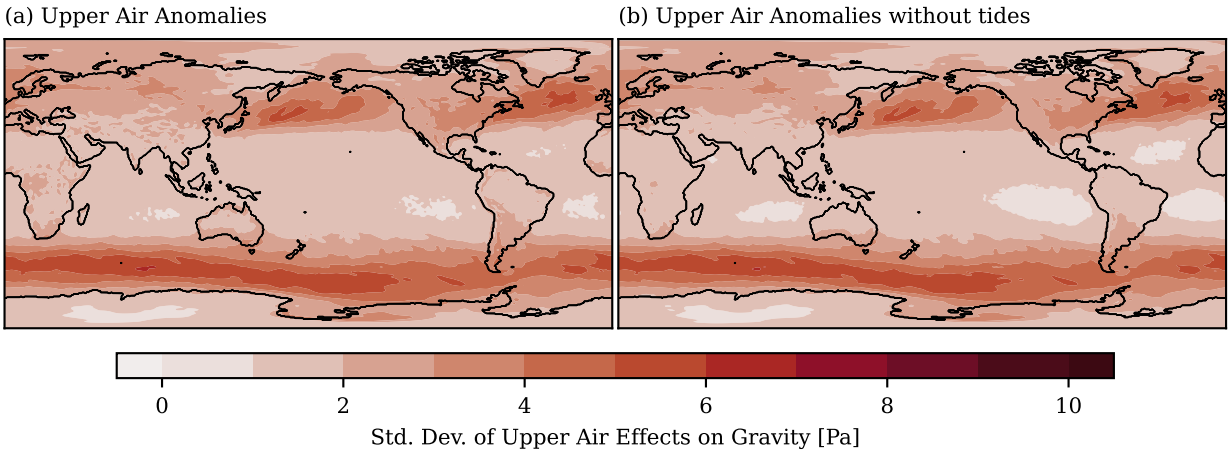

Figure 5.4: Sub-daily variability of upper air density anomalies expressed in equivalent surface pressure changes either including tidal signals (a) or after their removal (b).

5.4 Simulated Ocean Response to Atmospheric Tides

Periodic changes in atmospheric surface pressure over the oceans pose a time-variable loading to the water column that is not fully compensated isostatically, but excite a periodic motion in the oceans in addition to the contribution of lunisolar gravitational ocean tides. The MPIOM simulation used for AOD1B RL07 is forced with atmospheric conditions including atmospheric surface pressure obtained from ECMWF. By doing so, the oceanic response to atmospheric tides is implicitly simulated together with the transient non-tidal ocean circulation variability. However, the quality of the simulated tidal fields is affected by a number of limitations in the modelling approach as outlined below:

1. The atmospheric forcing is applied only every 1 or 3 hours and interpolated linearly to the internal model time-step so that atmospheric pressure variability at tidal frequencies is somewhat underestimated in many areas depending on the actual phase of the tidal wave in relation to the time-stepping of the atmospheric forcing.

2. The spatial resolution of MPIOM is only 1° on average, which is very coarse compared to current state-of-the-art tidal simulations. In particular the dynamics in semi-enclosed seas are often only poorly represented in such a setting.

3. Currently available model data-sets of the global ocean tides are either based on a combination of observations from satellite altimetry and other sources (GOT4.7, EOT11a); or hydrodynamic simulations that assimilate altimetry, gravimetry, or even tide gauge data (FES2014). MPIOM simulations for AOD1B, instead, do not assimilate any data but are governed by the applied atmospheric forcing only. In view of those limitations, we remove all tidal variability from the ocean component of AOD1B in the same way as for the atmospheric part.

The estimated and removed tidal signals from MPIOM are shown as a reference in Fig. 5.5.

Fig. 5.6 shows the sub-daily variability of MPIOM's ocean bottom pressure before (a) and after (b) the removal of the atmospherically induced tides.

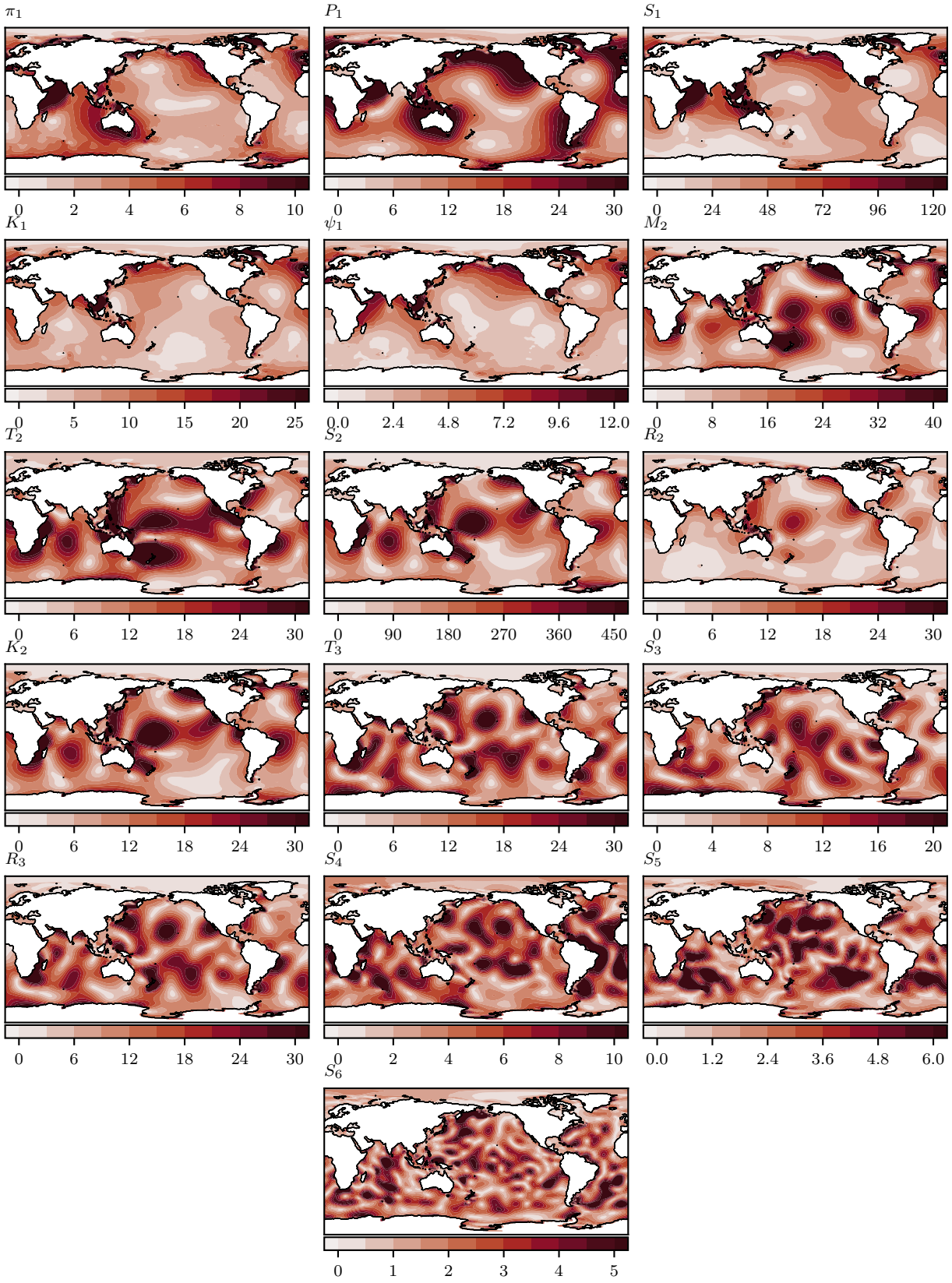

Figure 5.5: Exemplary surface pressure signals of atmospheric tides [Pa] for the tidal constituents removed from AOD1B RL07 as estimated over the year 2014.

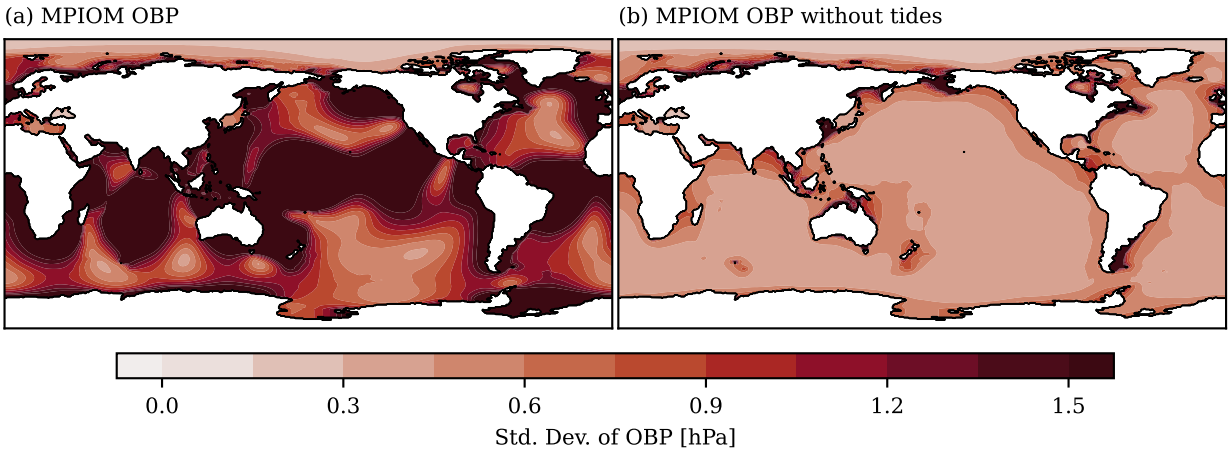

Figure 5.6: Sub-daily variability of MPIOM's ocean bottom pressure including tidal signals (a) or after their removal (b).

Chapter 6

AOD1B Low-Degree Stokes Coefficients

6.1 ATM and GAA Stokes Coefficients

The AOD1B non-tidal coefficients are provided in four individual components denoted as ATM, OCN, GLO, and OBA. The effects of the atmosphere are contained in the ATM coefficients that include the contribution of atmospheric surface pressure over the continents (Sect. 2.2); the static contribution of atmospheric pressure to ocean bottom pressure elsewhere (Sect. 2.4); and the much weaker contribution of upper-air density anomalies above both continents and oceans (Ch. 4). The monthly-means of the ATM coefficients are routinely provided together with the GRACE Level-2 gravity fields as GAA products.

Exemplarily, we provide time-series plots of the ATM low-degree spherical harmonic coefficients over the period 1975 – 2020 that are available from AOD1B RL07 (Fig. 6.1). High-frequency variability in C_{00} is substantially stronger during the years 1975 – 1978 where the so-called ERA5 Back-Extension data has been used. We further note a gradual increase in atmospheric mass which is plausible given the increased water holding capacity of a gradually warming atmosphere inline with the Clausius-Clapeyron Equation. We do not find any apparent jumps or inconsistencies. Similar conclusions are also drawn for the other coefficients.

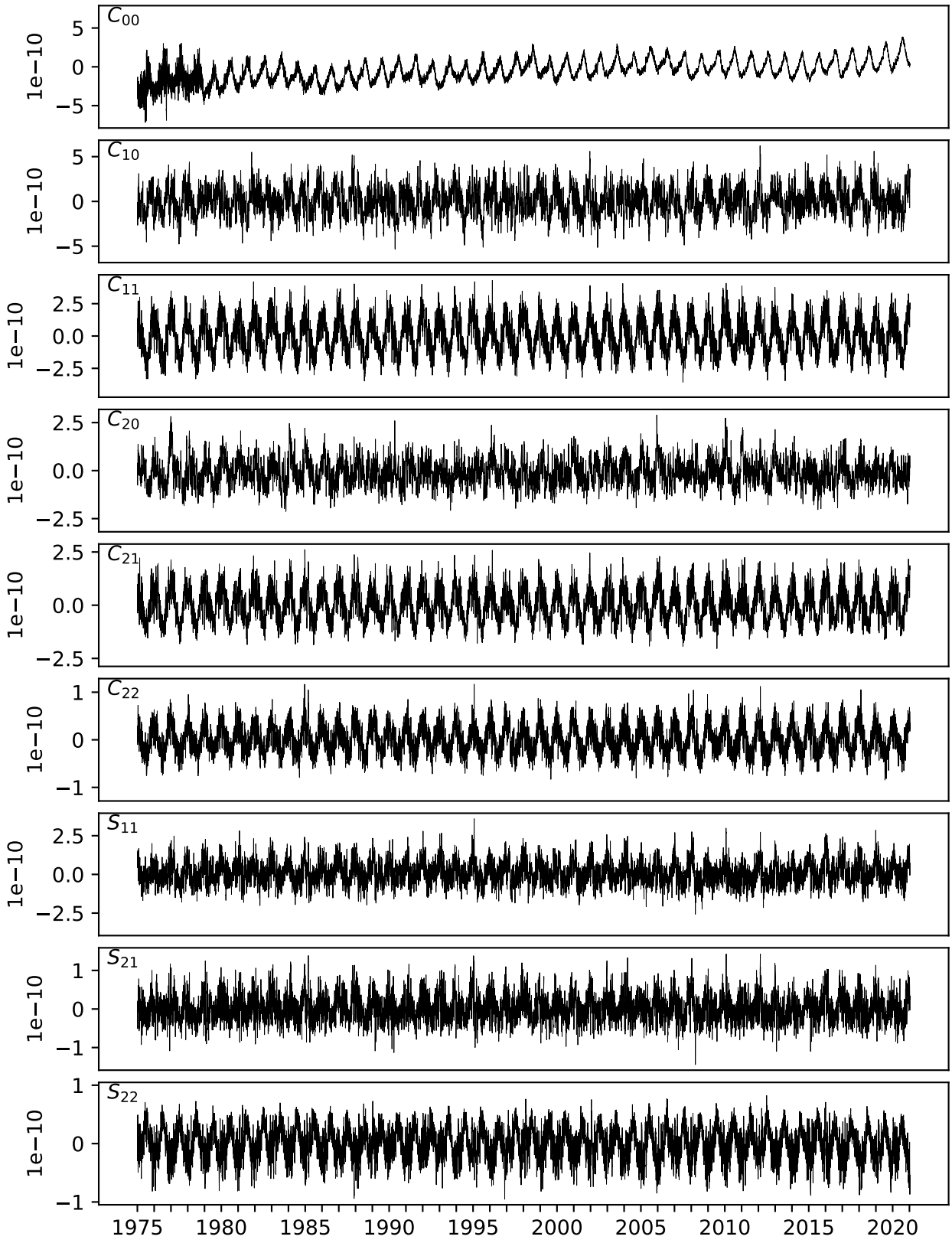

Figure 6.1: Time-series of ATM low-degree Stokes coefficients C_{00}, C_{10}, C_{11}, C_{20}, C_{21}, C_{22}, S_{11}, S_{21} and S_{22} of AOD1B RL07.

6.2 OCN and GAB Stokes Coefficients

The contribution of the dynamic ocean to ocean bottom pressure is provided as OCN as discussed in Ch. 3. The monthly-means of the OCN coefficients are routinely provided together with each GRACE Level-2 gravity field as the GAB product. Note that the static contribution of the atmosphere to ocean bottom pressure is excluded here.

We display time-series plots of the low-degree spherical harmonic coefficients over the period 1975 – 2021 for OCN (Fig. 6.2). Variability in C_{00} should be always zero due to the constraint imposed by applying eq. 3.1. Visual inspection of those coefficients displayed does not reveal any apparent jumps or inconsistencies.

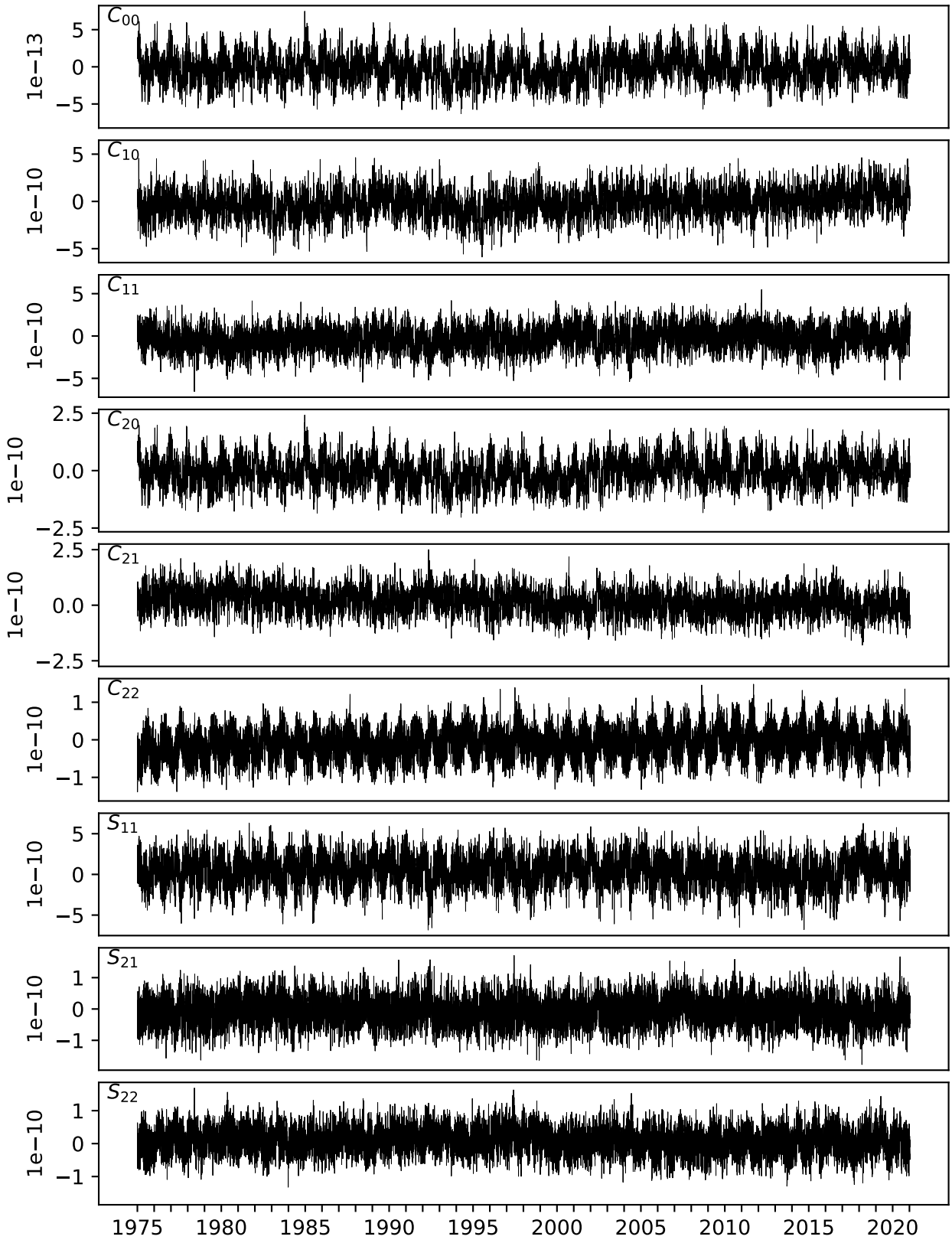

Figure 6.2: Time-series of OCN low-degree Stokes coefficients C_{00}, C_{10}, C_{11}, C_{20}, C_{21}, C_{22}, S_{11}, S_{21} and S_{22} of AOD1B RL07.

6.3 GLO and GAC Stokes Coefficients

The GLO coefficients are obtained from the sum of ATM and OCN at coefficient level. Those coefficients are usually applied in precise orbit determination. The monthly-means of the GLO coefficients are routinely provided together with the GRACE Level-2 gravity fields as GAC products.

We provide here time-series plots of the low-degree spherical harmonic GLO coefficients over the period 1975 – 2021 (Fig. 6.3). Variability in C_{00} reflects the time-variable atmospheric mass only since variations in oceanic mass are effectively zero at all times. The inspection of the other coefficients displayed does not reveal any artefacts.

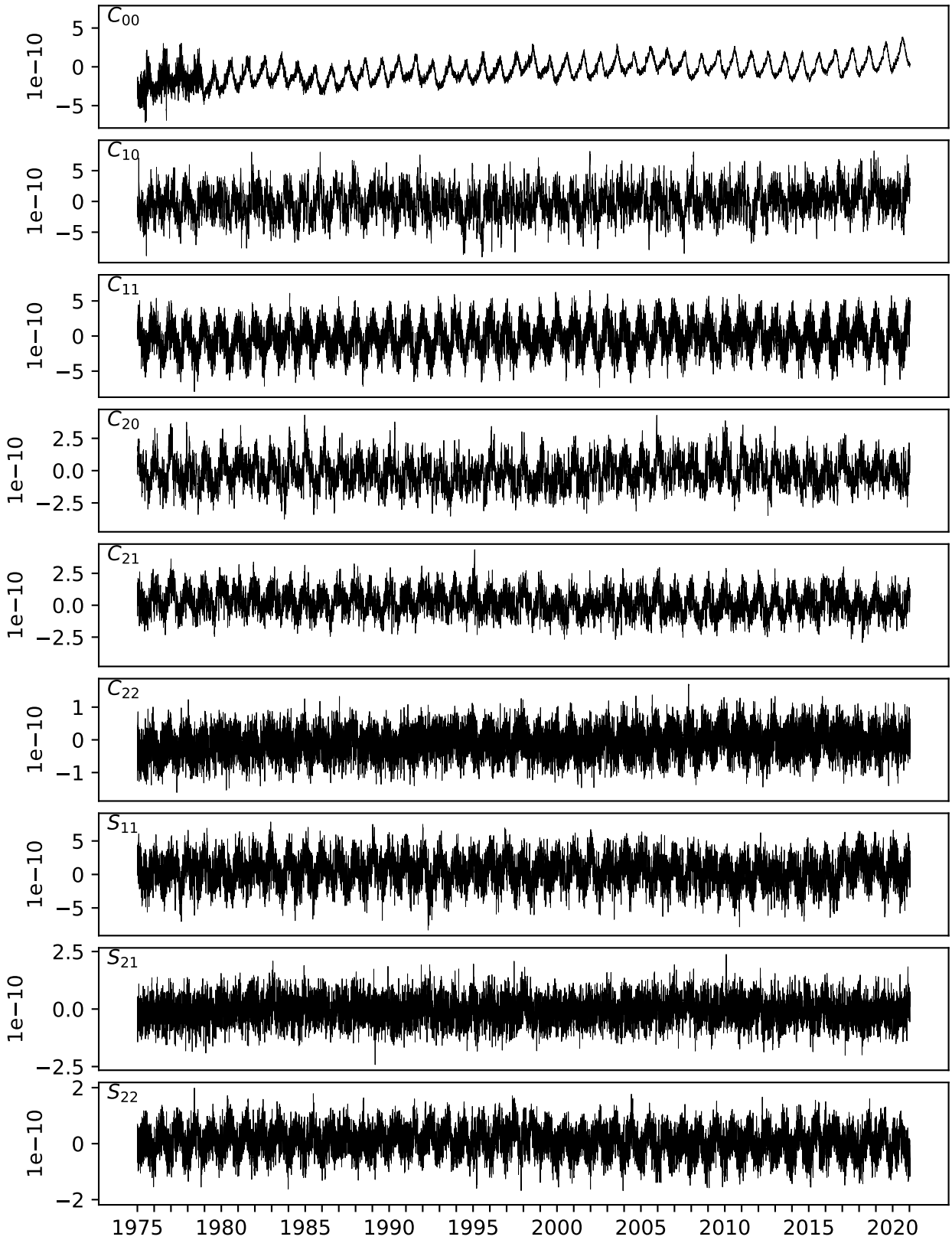

Figure 6.3: Time-series of GLO low-degree Stokes coefficients C_{00}, C_{10}, C_{11}, C_{20}, C_{21}, C_{22}, S_{11}, S_{21} and S_{22} of AOD1B RL07.

6.4 OBA and GAD Stokes Coefficients

The fourth set of AOD1B coefficients, OBA, is zero over the continents and provides the simulated ocean bottom pressure that includes air and water contributions elsewhere. Thus, OBA deviates from GLO over the ocean domain only by disregarding the small contribution of upper-air density anomaly contributions to the external gravity field. The monthly-means of the OBA coefficients are routinely provided together with any GRACE Level-2 gravity field as GAD product.

Time-series plots of the low-degree spherical harmonic coefficients over the period 1975 – 2021 are provided also for OBA (Fig. 6.4). Variations in C_{00} reflect the seasonal exchange of atmospheric mass between continental and oceanic regions regions, which is much larger than the drift in total atmospheric mass discussed before.

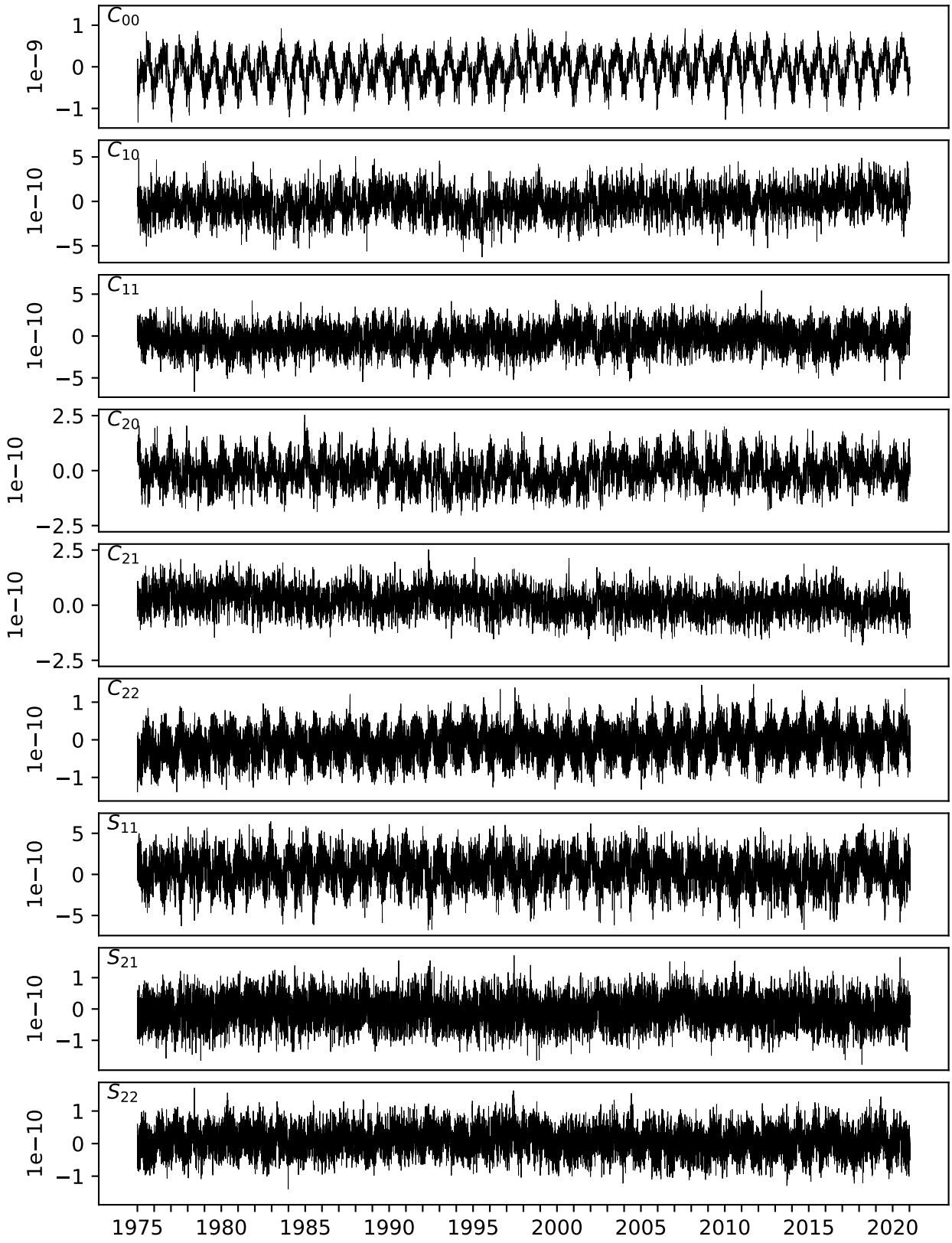

Figure 6.4: Time-series of OBA low-degree Stokes coefficients C_{00}, C_{10}, C_{11}, C_{20}, C_{21}, C_{22}, S_{11}, S_{21} and S_{22} of AOD1B RL07.

Chapter 7

Modelling Residual Uncertainties in AOD1B

AOD1B RL07 generally improves the representation of high-frequency non-tidal atmospheric and oceanic mass variations as shown in Shihora *et al.* (2022a). While this results in a reduction of temporal aliasing artefacts when applied in the gravity processing of satellite gravimetry, the background models remain imperfect to some extent. As a result, high-frequency signals not removed from the GRACE and GRACE-FO sensor data will lead to residual temporal aliasing artefacts in the monthly solutions. There are different approaches for mitigating the impact of residual aliasing errors in GRACE data processing. Most notably, several studies have shown that including an estimation of the uncertainty of the background model data can have a significant impact on the quality of the gravity field solutions. Kvas *et al.* (2019) suggested that including uncertainty estimations allows a weighting of the measurements according to the associated model error. As a result, measurements associated with a larger model uncertainty have a reduced contribution to the final gravity field solutions and therefore mitigate some of the effects from residual temporal aliasing.
To complement the AOD1B RL07 data, a new time-series of true errors, called AOe07, has been developed. AOe07 provides an estimation of the residual uncertainties in both the atmospheric and oceanic components of AOD1B that is compatible with RL07 and can be used both in the processing of satellite gravimetry measurements as well as in dedicated simulation studies in order to properly represent current background model capabilities. It replaces the AOerr series of the ESA ESM (Dobslaw *et al.*, 2016) which was representative for AOD1B RL05.

7.1 The AOe07 Time-Series of Synthetic Errors

The uncertainty estimation of AOe07 is performed for both the atmospheric component as well as the oceanic component. In both cases the uncertainties are calculated through model differences. For the atmosphere, we utilize 6 hourly surface pressure differences between the ERA5 reanalysis, as used in AOD1B RL07, and the MERRA2 reanalysis (Gelaro *et al.*, 2017). Both data-sets are initially remapped to a regular 0.5° grid following Dobslaw (2016) and tidal signals are estimated and removed individually.
The oceanic component is based on dedicated MPIOM simulations and combines the uncertainties in the forced variability, which is driven by the atmospheric forcing, as well as the intrinsic variability, caused by mesoscale turbulence (Serazin *et al.* (2015) and references therein) and other effects that are determined by the initial conditions. Two MPIOM simulations are performed: (a) a reference simulation based on ERA5 atmospheric forcing and an identical configuration to AOD1B

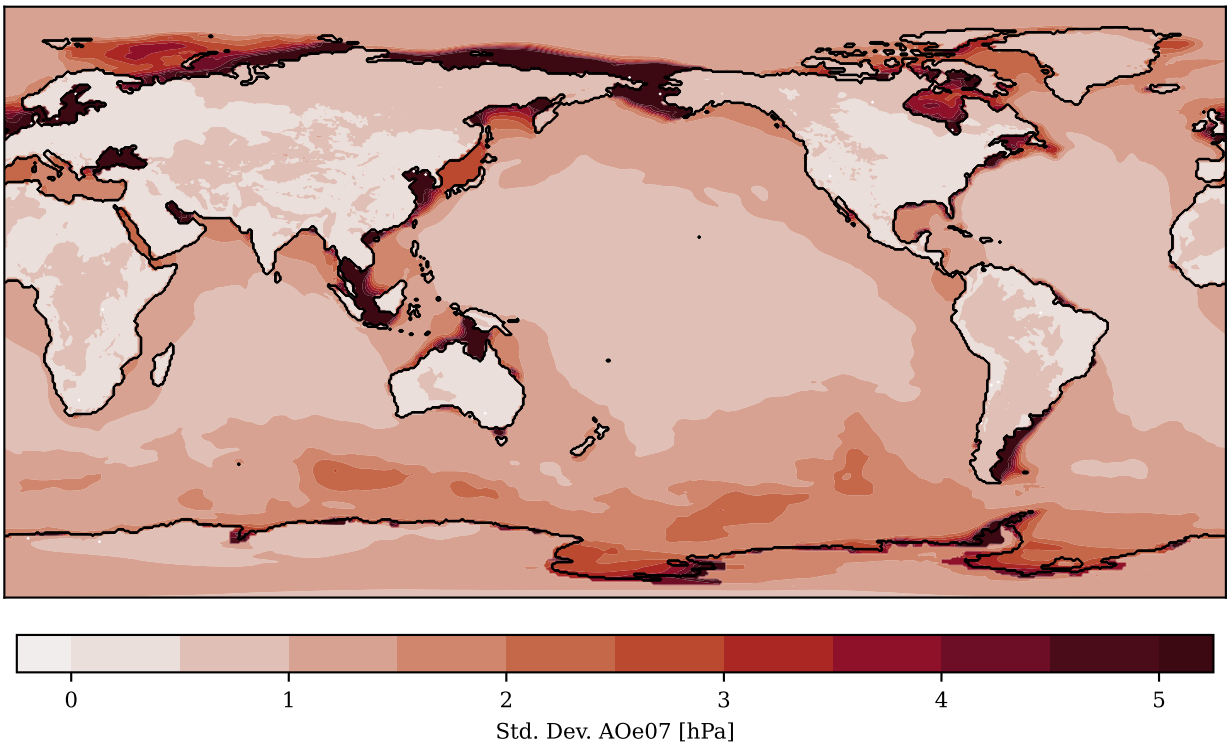

Figure 7.1: Standard deviation of the 6-hourly AOe07 timeseries resynthesized onto a regular grid.

RL07 except for the use of 3-hourly atmospheric forcing and (b) a simulation based on 3-hourly MERRA2 forcing with the initial conditions shifted by one year from 1994 to 1993. In both simulations, OBP fields are extracted and post-processed individually in the same way as the OBP data used in AOD1B including the removal of atmospherically induced tidal signals. The difference of the two OBP time-series is used as the basis of the oceanic component of AOe07. As, however, ocean model differences using the same ocean model tend to underestimate the high-frequency variations (Quinn & Ponte, 2011) a constant scaling factor of 2.4 is applied to the OBP differences. This factor is based on a comparison of the unscaled OBP differences to the residual variability of daily GRACE solutions as described in Shihora *et al.* (2023c).
The final AOe07 time-series is based on the surface pressure differences over the continents and the OBP differences over the ocean domain. Atmospheric tidal signals in both the atmosphere and ocean are removed from each contribution separately as described in Sect. 5. The time-series is high-pass filtered using a 4th order Butterworth filter and a cut-off frequency of 30 days. The dataset covers the years 1995 – 2020, is supplied as 6-hourly Stokes coefficients up to d/o 180 and can be accessed via the ESA ESM repository.

Fig. 7.1 shows the variability of the final AOe07 time-series after resynthesizing the coefficients back onto a regular 0.5° grid.

7.2 Stationary Error-Variance-Covariance Matrix for AOD1B RL07

An alternative way to include the errors of background models is through the use of an error-variance-covariance matrix (VCM) which represents the spatio-temporal uncertainties. Such a VCM can then be used either in the gravity field estimation process or in dedicated simulation studies as shown by Abrykosov *et al.* (2021); Hauk *et al.* (2023) for the case of ocean tides.

The calculation of the VCM is based on the computation of both variances as well as covariances between the Stokes coefficients via

$$\mathrm{cov}(X_{l_1,m_1}, X_{l_2,m_2}) = \frac{1}{N_t - 1} \sum_t (X_{l_1,m_1} - \overline{X}_{l_1,m_1}) \cdot (X_{l_2,m_2} - \overline{X}_{l_2,m_2}) \tag{7.1}$$

where X_{l_1,m_1} stands for the C and S Stokes coefficients of degree l_1 and order m_1 while $\overline{X}$ represents the temporal mean value. Variances are computed analogously using $l_1 = l_2$ and $m_1 = m_2$. Based on Eq. 7.1 a fully populated stationary VCM is calculated up to d/o 40. This matches the resolution of current GRACE daily solutions such as ITSG2018 (Mayer-Gürr *et al.*, 2018; Kvas *et al.*, 2019). Additionally, a second diagonal matrix, containing thus only variances, is calculated up to the full d/o 180. Both matrices are publicly available under Shihora *et al.* (2023a).

Chapter 8

User Recommendations

8.1 AOD1B in Precise Orbit Determination

For the application of AOD1B as a time-variable background model in precise orbit determination, we recommend linear interpolation between two consecutive time-steps of the 3-hourly non-tidal GLO coefficients to arrive at the anomalous gravity field at an arbitrary time epoch.

While there are no atmospheric tidal signal supplied under the AOD1B RL07 directory, dedicated tidal estimations based on the ERA5 reanalysis, which are consistent with the removed signals of AOD1B RL07, are available under Sulzbach *et al.* (2022). In case that atmospheric tidal models based on surface pressure station observations are readily available for selected frequencies as, e.g., presented by Schindelegger & Ray (2014) for S_1 and S_2, those might be given preference over the tidal signals provided.

Since the oceanic response to the atmospheric tidal signals is not well captured in MPIOM. As explained in Ch. 5, the oceanic response to these signals is available separately from Sulzbach *et al.* (2022) as well and is based on dedicated simulations with the barotropic ocean tide model TiME (Sulzbach *et al.*, 2021). Further details on atmospherically forced ocean tides are provided in Balidakis *et al.* (2022).

8.2 Ocean Bottom Pressure and Sea-Level Variations

Users interested in deriving ocean bottom pressure variations out of the GRACE Level-2 coefficients are advised to re-add GAD to the monthly GSM gravity fields in order to restore the part of the monthly-mean bottom pressure signal removed during de-aliasing. The restore step should be performed only after applying non-isotropic filters as developed by, e.g., Swenson & Wahr (2006) or Kusche (2007) to the GSM coefficients. Note that effects from upper-air atmospheric density anomalies as described in Ch. 4 are not restored in this case, which are part of GAC but not part of GAD over oceanic regions.

In order to estimate mass-induced sea-level variations from the GRACE gravity fields, users should alternatively consider to re-add GAB instead of GAD. By doing so, only the gravitational signals of the ocean water masses are restored, whereas the IB-corrected effects of the atmospheric surface pressure and the contributions of upper-air atmospheric mass variability are kept separated.

Users specifically interested in estimating the global mean barystatic sea-level change are advised that the total mass of the oceanic component of the de-aliasing product (i.e., GAB) is kept constant at all time-steps. For an integration over all oceanic regions it is therefore recommended to consider

GSM only without restoring any of the components of AOD1B. In all cases, we do not recommend restoring any of the tidal signals originating from oceans, atmosphere, or the solid Earth. As recommended before, any restore step should be performed only after applying a non-isotropic filter from Swenson & Wahr (2006) or Kusche (2007).

8.3 Global Mass Re-Distribution and Atmospheric Applications

Users specifically interested in studying global mass re-distributions in the Earth system including all mass variability in atmosphere and oceans from GRACE gravity fields are advised to re-add GAC to the monthly GSM products. The restore step should be performed only after applying non-isotropic filters as developed by, e.g., Swenson & Wahr (2006) or Kusche (2007) to the GSM coefficients. We do not recommend restoring any of the tidal signals originating from oceans, atmosphere, or the solid Earth.

For studies on atmospheric contributions to the time-variable gravity field, users are advised that the ATM coefficients and the corresponding monthly mean GAA products apply an inverse-barometric correction over the oceans (see Sect. 2.4), and are thus approximately comparable to in situ surface pressure observations only in continental regions away from the coasts.

8.4 Hydrospheric, Cryospheric, and Tectonic Applications

For typical hydrospheric, cryospheric, or tectonic applications, GRACE monthly GSM gravity field products can be used as delivered by the processing centres. There is no need to restore any of the signals removed during the de-aliasing process.

References

Abrykosov, P., Sulzbach, R., Pail, R., Dobslaw, H. & Thomas, M. (2021). Treatment of ocean tide background model errors in the context of GRACE/GRACE-FO data processing, *Geophysical Journal International*, **228**, 1850-1865, DOI:10.1093/gji/ggab421. 50

Balidakis, K., Sulzbach, R., Dobslaw, H. & Dill, R. (2023). *How Do Atmospheric Tidal Loading Displacements Vary Temporally as well as Across Different Weather Models?*, Springer Berlin Heidelberg, Berlin, Heidelberg, p. 1–9, DOI:10.1007/1345_2023_201. 34

Balidakis, K., Sulzbach, R., Shihora, L., Dahle, C., Dill, R. & Dobslaw, H. (2022). Atmospheric Contributions to Global Ocean Tides for Satellite Gravimetry, *Journal of Advances in Modeling Earth Systems*, **14**, DOI:10.1029/2022MS003193. 33, 53

Bell, B., Hersbach, H., Simmons, A., Berrisford, P., Dahlgren, P., Horányi, A., Munoz-Sabater, J., Nicolas, J., Radu, R., Schepers, D., Soci, C., Villaume, S., Bidlot, J.-R., Haimberger, L., Woollen, J., Buontempo, C. & Thepaut, J.-N. (2021). The ERA5 global reanalysis: Preliminary extension to 1950, *Quarterly Journal of the Royal Meteorological Society*, **147**, 4186-4227, DOI:10.1002/qj.4174. 19

Bergmann, I. & Dobslaw, H. (2012). Short-term transport variability of the Antarctic Circumpolar Current from satellite gravity observations, *J. Geophys. Res.*, **117**, 1–12, DOI:10.1029/2012JC007872. 23

Bettadpur, S., Flechtner, F. & Schmidt, R. (2006). Technical Note 04 - Usage Guidelines for GFZ RL03 and JPL RL02 Grace Gravity Fields & Atmosphere/Ocean Background Models - Version 1.1, www.isdc.gfz-potsdam.de. 9

Blewitt, G. (2003). Self-consistency in reference frames, geocenter definition, and surface loading of the solid Earth, *J. Geophys. Res.*, **108**, DOI:10.1029/2002JB002082. 16

Boy, J.-P. & Chao, B. F. (2005). Precise evaluation of atmospheric loading effects on Earth's time-variable gravity field, *J. Geophys. Res.*, **110**, 1–10, DOI:10.1029/2002JB002333. 13, 14

Case, K., Kruizinga, G. & Wu, S. (2002). *GRACE Level 1B Data Product User Handbook*, JPL Publication D-22027. 61, 65

Dee, D. P., Uppala, S. M., Simmons, A. J., Berrisford, P., Poli, P., Kobayashi, S., Andrae, U., Balmaseda, M. A., Balsamo, G., Bauer, P., Bechtold, P., Beljaars, A. C. M., van de Berg, L., Bidlot, J., Bormann, N., Delsol, C., Dragani, R., Fuentes, M., Geer, A. J., Haimberger, L., Healy, S. B., Hersbach, H., Hólm, E. V., Isaksen, L., Kallberg, P., Köhler, M., Matricardi, M., McNally, A. P., Monge-Sanz, B. M., Morcrette, J.-J., Park, B.-K., Peubey, C., de Rosnay, P., Tavolato, C., Thépaut, J.-N. & Vitart, F. (2011). The ERA-Interim reanalysis: configuration and performance of the data assimilation system, *Q. J. Roy. Meteor. Soc.*, **137**, 553–597, DOI:10.1002/qj.828. 9, 10

Dobslaw, H. (2016). Homogenizing surface pressure time-series from operational numerical weather prediction models for geodetic applications, *J. Geod. Sci.*, **6**, 61–68, DOI:10.1515/jogs-2016-0004. 49

Dobslaw, H., Bergmann-Wolf, I., Forootan, E., Dahle, C., Mayer-Gürr, T., Kusche, J. & Flechtner, F. (2016). Modeling of present-day atmosphere and ocean non-tidal de-aliasing errors for future gravity mission simulations, *Journal of Geodesy*, **90**, 423-436, DOI:10.1007/s00190-015-0884-3. 49

Dobslaw, H., Dill, R., Grötzsch, A., Brzeziński, A. & Thomas, M. (2010). Seasonal polar motion excitation from numerical models of atmosphere, ocean, and continental hydrosphere, *J. Geophys. Res.*, **115**, B10406, DOI:10.1029/2009JB007127. 21

Dobslaw, H., Flechtner, F., Bergmann-Wolf, I., Dahle, C., Dill, R., Esselborn, S., Sasgen, I. & Thomas, M. (2013). Simulating high-frequency atmosphere-ocean mass variability for dealiasing of satellite gravity observations: AOD1B RL05, *J. Geophys. Res.*, **118**, 3704-3711, DOI:10.1002/jgrc.20271. 9

Dobslaw, H. & Thomas, M. (2005). Atmospheric induced oceanic tides from ECMWF forecasts, *Geophys. Res. Lett.*, **32**, L10615, DOI:10.1029/2005GL022990. 11

Dobslaw, H. & Thomas, M. (2007). Simulation and observation of global ocean mass anomalies, *J. Geophys. Res.*, **112**, C05040, DOI:10.1029/2006JC004035. 9

Dong, D., Gross, R. & Dickey, J. (1996). Seasonal variations of the Earth's gravitational field: An analysis of atmospheric pressure, ocean tidal, and surface water excitation, *Geophys. Res. Lett.*, **23**, 725–728, DOI:10.1029/96gl00740. 16

Drijfhout, S., Heinze, C., Latif, M. & Maier-Reimer, E. (1996). Mean Circulation and Internal Variability in an Ocean Primitive Equation Model, *J. Phys. Oceanogr.*, **26**, 559–580, DOI:10.1175/1520-0485(1996)026<0559:MCAIVI>2.0.CO;2. 21

Flechtner, F., Thomas, M. & König, R. (2008). *A long-term model for non-tidal atmospheric and oceanic mass redistributions and its implications on LAGEOS-derived solutions of Earth's oblateness (Scientific Technical Report STR ; 08/12)*, *Tech. rep.*, Potsdam: Deutsches GeoForschungsZentrum GFZ, DOI:10.2312/GFZ.b103-08123. 9

Gelaro, R., McCarty, W., SuÃ¡rez, M. J., Todling, R., Molod, A., Takacs, L., Randles, C. A., Darmenov, A., Bosilovich, M. G., Reichle, R., Wargan, K., Coy, L., Cullather, R., Draper, C., Akella, S., Buchard, V., Conaty, A., da Silva, A. M., Gu, W., Kim, G.-K., Koster, R., Lucchesi, R., Merkova, D., Nielsen, J. E., Partyka, G., Pawson, S., Putman, W., Rienecker, M., Schubert, S. D., Sienkiewicz, M. & Zhao, B. (2017). The Modern-Era Retrospective Analysis for Research and Applications, Version 2 (MERRA-2), *Journal of Climate*, **30**, 5419 - 5454, DOI:10.1175/JCLI-D-16-0758.1. 49

Greatbatch, R. (1994). A note on the representation of steric sea level in models that conserve volume rather than mass, *J. Geophys. Res.*, **99**, 12767-12771, DOI:10.1029/94JC00847. 22

Hartmann, T. & Wenzel, H.-G. (1995). The HW95 tidal potential catalogue, *Geophysical Research Letters*, **22**, 3553–3556, DOI:https://doi.org/10.1029/95GL03324, URL https://agupubs.onlinelibrary.wiley.com/doi/abs/10.1029/95GL03324, https://agupubs.onlinelibrary.wiley.com/doi/pdf/10.1029/95GL03324. 34

Hasselmann, K. (2013). Ernst Maier-Reimer: The discovery of silence, *Nature Geoscience*, **6**, 809–809, DOI:10.1038/ngeo1953. 21

Hauk, M., Wilms, J., Sulzbach, R., Panafidina, N., Hart-Davis, M., Dahle, C., Müller, V., Murböck, M. & Flechtner, F. (2023). Satellite gravity field recovery using variance-covariance information from ocean tide models, *Earth and Space Science*, **10**, e2023EA003098, DOI: 10.1029/2023EA003098. 50

Heiskanen, W. & Moritz, H. (1967). *Physical Geodesy*, Freeman, San Francisco. 7

Hersbach, H., Bell, B., Berrisford, P., Hirahara, S., Horányi, A., Muñoz-Sabater, J., Nicolas, J., Peubey, C., Radu, R., Schepers, D., Simmons, A., Soci, C., Abdalla, S., Abellan, X., Balsamo, G., Bechtold, P., Biavati, G., Bidlot, J., Bonavita, M., De Chiara, G., Dahlgren, P., Dee, D., Diamantakis, M., Dragani, R., Flemming, J., Forbes, R., Fuentes, M., Geer, A., Haimberger, L., Healy, S., Hogan, R. J., Hólm, E., Janisková, M., Keeley, S., Laloyaux, P., Lopez, P., Lupu, C., Radnoti, G., de Rosnay, P., Rozum, I., Vamborg, F., Villaume, S. & Thépaut, J.-N. (2020). The ERA5 global reanalysis, *Quarterly Journal of the Royal Meteorological Society*, **146**, 1999-2049, DOI:10.1002/qj.3803. 11

Hibler, W. (1979). A Dynamic Thermodynamic Sea Ice Model, *J. Phys. Oceanogr.*, **9**, 815–846, DOI:10.1175/1520-0485(1979)009<0815:ADTSIM>2.0.CO;2. 21

Hirose, N., Fukumori, I., Zlotnicki, V. & Ponte, R. (2001). Modeling the high-frequency barotropic response of the ocean to atmospheric disturbances: Sensitivity to forcing, topography, and friction, *J. Geophys. Res.*, **106**, 30987-30995, DOI:10.1029/2000JC000763. 9

Jungclaus, J. H., Fischer, N., Haak, H., Lohmann, K., Marotzke, J., Matei, D., Mikolajewicz, U., Notz, D. & von Storch, J. S. (2013). Characteristics of the ocean simulations in the Max Planck Institute Ocean Model (MPIOM) the ocean component of the MPI-Earth system model, *Journal of Advances in Modeling Earth Systems*, **5**, 422–446, DOI:10.1002/jame.20023. 7, 10, 21

Kusche, J. (2007). Approximate decorrelation and non-isotropic smoothing of time-variable GRACE-type gravity field models, *J. Geod.*, **81**, 733–749, DOI:10.1007/s00190-007-0143-3. 53, 54

Kvas, A., Behzadpour, S., Ellmer, M., Klinger, B., Strasser, S., Zehentner, N. & Mayer-GÃ¼rr, T. (2019). ITSG-Grace2018: Overview and Evaluation of a New GRACE-Only Gravity Field Time Series, *Journal of Geophysical Research: Solid Earth*, **124**, 9332-9344, DOI:10.1029/2019JB017415. 49, 51

Landerer, F. W., Flechtner, F. M., Save, H., Webb, F. H., Bandikova, T., Bertiger, W. I., Bettadpur, S. V., Byun, S. H., Dahle, C., Dobslaw, H., Fahnestock, E., Harvey, N., Kang, Z., Kruizinga, G. L. H., Loomis, B. D., McCullough, C., Murböck, M., Nagel, P., Paik, M., Pie, N., Poole, S., Strekalov, D., Tamisiea, M. E., Wang, F., Watkins, M. M., Wen, H.-Y., Wiese, D. N. & Yuan, D.-N. (2020). Extending the Global Mass Change Data Record: GRACE Follow-On Instrument and Science Data Performance, *Geophysical Research Letters*, **47**, DOI:10.1029/2020GL088306. 7

Levitus, S. (2005). Warming of the world ocean, 1955–2003, *Geophys. Res. Lett.*, **32**, 1–4, DOI: 10.1029/2004GL021592. 22

Maier-Reimer, E. & Mikolajewicz, U. (1992). *The Hamburg Large Scale Geostrophic Ocean General Circulation Model Cycle 1, Tech. Rep. 2*, Deutsches Klimarechenzentrum, Hamburg. 21

Marsland, S. J., Haak, H., Jungclaus, J., Latif, M. & Röske, F. (2003). The Max-Planck-Institute global ocean/sea ice model with orthogonal curvilinear coordinates, *Ocean Modelling*, **5**, 91–127, DOI:10.1016/S1463-5003(02)00015-X. 21

Mayer-Gürr, T., Behzadpour, S., Ellmer, M., Kvas, A., Klinger, B., Strasser, S. & Zehentner, N. (2018). ITSG-Grace2018 - Monthly, Daily and Static Gravity Field Solutions from GRACE, *GFZ Data Services*, DOI:10.5880/ICGEM.2018.003. 51

Notz, D., Haumann, F. A., Haak, H., Jungclaus, J. H. & Marotzke, J. (2013). Arctic sea-ice evolution as modeled by Max Planck Institute for Meteorology's Earth system model, *J. Adv. Model. Earth Sy.*, **5**, 173-194, DOI:10.1002/jame.20016. 21

Petit, G. & Luzum, B. (2010). *IERS Convention (2010) (IERS Technical Note no. 36)*, *Tech. rep.*, Verlag des Bundesamtes für Kartographie und Geodäsie, Frankfurt am Main, URL http://www.iers.org/IERS/EN/Publications/TechnicalNotes/tn36.html. 14, 15

Quinn, K. J. & Ponte, R. M. (2011). Estimating high frequency ocean bottom pressure variability, *Geophysical Research Letters*, **38**, DOI:10.1029/2010GL046537. 50

Ray, R. D. & Egbert, G. D. (2004). The Global S 1 Tide, *J. Phys. Oceanogr.*, **34**, 1922–1935, DOI:10.1175/1520-0485(2004)034<1922:TGST>2.0.CO;2. 34

Ray, R. D. & Ponte, R. M. (2003). Barometric tides from ECMWF operational analyses, *Annales Geophysicae*, **21**, 1897–1910, DOI:10.5194/angeo-21-1897-2003. 9

Ray, R. D. & Poulose, S. (2005). Terdiurnal surface-pressure oscillations over the continental United States, *Mon. Weather Rev.*, **133**, 2526-2534, DOI:10.1175/MWR2988.1. 34

Reigber, C., Balmino, G., Schwintzer, P., Biancale, R., Bode, A., Lemoine, J.-M., Ko, R., Loyer, S., Neumayer, K.-H., Marty, J.-C., Barthelmes, F., Perosanz, F. & Zhu, S. Y. (2002). A High-Quality Global Gravity Field Model from CHAMP GPS Tracking Data and Accelerometry (EIGEN-1S), *Geophys. Res. Lett.*, **29**, 94–97, DOI:10.1029/2002GL015064. 7

Röske, F. (2005). *Global oceanic heat and fresh water forcing datasets based on ERA-40 and ERA-15 Reports on Earth System Science*, *Reports on Earth System Science 13*, Max Planck Institute for Meteorology, URL www.mpimet.mpg.de. 22

Rummel, R., Yi, W. & Stummer, C. (2011). GOCE gravitational gradiometry, *J. Geod.*, **85**, 777-790, DOI:10.1007/s00190-011-0500-0. 7

Schindelegger, M. & Ray, R. D. (2014). Surface Pressure Tide Climatologies Deduced from a Quality-Controlled Network of Barometric Observations, *Mon. Weather Rev.*, **142**, 4872-4889, DOI:10.1175/MWR-D-14-00217.1. 33, 53

Serazin, G., Penduff, T., Grégorio, S., Barnier, B., Molines, J.-M. & Terray, L. (2015). Intrinsic Variability of Sea Level from Global Ocean Simulations: Spatiotemporal Scales, *Journal of Climate*, **28**, 4279 - 4292, DOI:10.1175/JCLI-D-14-00554.1. 49

Shihora, L., Balidakis, K., Dill, R., Dahle, C., Ghobadi-Far, K., Bonin, J. & Dobslaw, H. (2022a). Non-Tidal Background Modeling for Satellite Gravimetry Based on Operational ECWMF and ERA5 Reanalysis Data: AOD1B RL07, *Journal of Geophysical Research: Solid Earth*, **127**, DOI:10.1029/2022JB024360. 49

Shihora, L., Balidakis, K., Dill, R. & Dobslaw, H. (2023a). AOe07 Variance-Covariance-Matrix, DOI:10.5880/nerograv.2023.004, GFZ Data Services. 51

Shihora, L., Balidakis, K., Dill, R. & Dobslaw, H. (2023b). Assessing the stability of AOD1B atmosphere-ocean non-tidal background modelling for climate applications of satellite gravity data: long-term trends and 3-hourly tendencies, *Geophysical Journal International*, **234**, 1063-1072, DOI:10.1093/gji/ggad119. 25

Shihora, L., Liu, Z., Balidakis, K., Wilms, J., Dahle, C., Flechtner, F., Dill, R. & Dobslaw, H. (2023c). Accounting for Residual Errors in Atmosphere-Ocean Background Models Applied in Satellite Gravimetry, *under review at Journal of Geodesy*. 50

Shihora, L., Sulzbach, R., Dobslaw, H. & Thomas, M. (2022b). Self-attraction and loading feedback on ocean dynamics in both shallow water equations and primitive equations, *Ocean Modelling*, **169**, 101914, DOI:10.1016/j.ocemod.2021.101914. 21

Simon, B. (2013). *Coastal Tides*, Synthèses - Institut océanographique, Institut océanographique éd., URL https://books.google.de/books?id=oQjsoAEACAAJ. 34

Sulzbach, R., Balidakis, K., Dobslaw, H. & Thomas, M. (2022). TiME22: Periodic disturbances of the terrestrial gravity potential induced by oceanic and atmospheric tides, DOI:https://doi.org/10.5880/GFZ.1.3.2022.006. 53

Sulzbach, R., Dobslaw, H. & Thomas, M. (2021). High-resolution numerical modeling of barotropic global ocean tides for satellite gravimetry, *Journal of Geophysical Research: Oceans*, **126**, e2020JC017097, DOI:10.1029/2020JC017097. 53

Swenson, S. & Wahr, J. (2002). Estimated effects of the vertical structure of atmospheric mass on the time-variable geoid, *J. Geophys. Res.*, **107**, DOI:10.1029/2000JB000024. 13, 15

Swenson, S. C. & Wahr, J. M. (2006). Post-processing removal of correlated errors in GRACE data, *Geophys. Res. Lett.*, **33**, 1–4, DOI:10.1029/2005GL025285. 53, 54

Tapley, B., Bettadpur, S., Watkins, M. & Reigber, C. (2004). The gravity recovery and climate experiment: Mission overview and early results, *Geophys. Res. Lett.*, **31**, L09607, DOI:10.1029/2004GL019920. 7

Thomas, M. & Dobslaw, H. (2004). On the impact of baroclinic ocean dynamics on the Earth's gravity field, in: *Joint CHAMP/GRACE Science Team Meeting, Potsdam*, URL http://gfzpublic.gfz-potsdam.de/pubman/item/escidoc:239639. 9

Uppala, S., Kallberg, P., Simmons, A., Andrae, U., Bechtold, V. & et al. (2005). The ERA-40 re-analysis, *Q. J. R. Meteorol. Soc.*, **131**, 2961–3012, DOI:10.1256/qj.04.176. 9, 10

Wahr, J. M., Molenaar, M. & Bryan, F. (1998). Time variability of the Earth's gravity field: Hydrological and oceanic effects and their possible detection using GRACE, *J. Geophys. Res.*, **103**, 30205, DOI:10.1029/98JB02844. 13, 17

Wang, H., Wu., P. & Wang, Z. (2006). An approach for spherical harmonic analysis of non-smooth data, *Computer & Geosciences*, **32**, 1654-1668, DOI:10.1016/j.cageo.2006.03.004. 15, 16

Wolff, J.-O., Maier-Reimer, E. & Legutke, S. (1997). *The Hamburg Ocean Primitive Equation Model HOPE, Tech. Rep. 13*, URL http://mms.dkrz.de/pdf/klimadaten/models/ReportNo.13.pdf. 21

Wunsch, C. & Stammer, D. (1997). Atmospheric Loading and the Oceanic "Inverted Barometer" Effect, *Rev. Geophys.*, **35**, 79–107, DOI:10.1029/96RG03037. 13

Yessad, K. (2015). *FULL-POS in the Cycle 41T1 of ARPEGE/IFS, Tech. rep.*, Meteo-France, URL http://www.cnrm.meteo.fr/gmapdoc/IMG/pdf/ykfpos41t1.pdf. 11, 12

Appendix A

AOD1B Non-Tidal Coefficients Format Description and Download

Non-tidal AOD1B files are available from the GRACE data repository maintained by GFZ via `ftp://isdcftp.gfz-potsdam.de/grace/Level-1B/GFZ/AOD/RL07`. The corresponding DOI is `https://doi.org/10.5880/GFZ.1.3.2022.003`.

Format and content of the **non-tidal coefficients** of AOD1B are described in the following. The files are updated daily in the GRACE archives by using the GRACE Level-1 filename convention "AOD1B_YYYY-MM-DD_S_RL.EXT.gz" (Case *et al.*, 2002), where "YYYY-MM-DD" is the corresponding date, the GRACE satellite identifier "S" is fixed to X implying that the product is not referring to a particular spacecraft; "RL" is an increasing release number, and EXT is fixed to "asc" indicating that the file is provided in plain text. For data transfer speed-up, the products are gnu-zipped.

Each file consists of a header with a dedicated number of lines ("NUMBER OF HEADER RECORDS") and ends with a constant header line ("END OF HEADER"). The first part of the header is based on the Level-1 instrument product header convention (Case *et al.*, 2002) and gives more general information on the product (header lines "PRODUCER AGENCY" to "PROCESS LEVEL"). These lines are followed by a number of header lines describing the de-aliasing product more precisely:

```
PRESSURE TYPE (SP OR VI)        : surface pressure or vertical integration approach
MAXIMUM DEGREE                  : maximum degree of the spherical harmonic series
COEFFICIENT ERRORS (YES/NO)     : yes, if errors are given for each coefficient
COEFF. NORMALIZED (YES/NO)      : yes, if the coefficients are normalized
CONSTANT GM [M^3/S^2]           : GM value used for computation
CONSTANT A [M]                  : semi-major axis value used for computation
CONSTANT FLAT [-]               : flattening value used for computation
CONSTANT OMEGA [RAD/S]          : Earth rotation rate used for computation
NUMBER OF DATA SETS             : number of data fields per product file
DATA FORMAT (N,M,C,S)           : format string to read the data
```

The "NUMBER OF DATA SETS" is 12 (RL04), 16 (RL05) and 32 (RL06 & RL07) depending on the temporal resolution and the number of coefficient sets (ATM, OCN, GLO, OBA) considered. The "MAXIMUM DEGREE" is set to 180.

The following is an example for a single AOD1B RL07 product file, where for simplification only the two first coefficients of each data set are given:

```
PRODUCER AGENCY                : GFZ
PRODUCER INSTITUTION           : GFZ
FILE TYPE ipAOD1BF             : 999
FILE FORMAT 0=BINARY 1=ASCII   : 1
NUMBER OF HEADER RECORDS       : 29
SOFTWARE VERSION               : atm_ocean_dealise.07_v1
SOFTWARE LINK TIME             : Not Applicable
REFERENCE DOCUMENTATION        : GRACE AOD1B PDD
SATELLITE NAME                 : GRACE X
SENSOR NAME                    : Not Applicable
TIME EPOCH (GPS TIME)          : 2000-01-01 12:00:00
TIME FIRST OBS(SEC PAST EPOCH): 389102400.000000 (2012-05-01 00:00:00)
TIME LAST OBS(SEC PAST EPOCH) : 389178000.000000 (2012-05-01 21:00:00)
NUMBER OF DATA RECORDS         : 527072
PRODUCT CREATE START TIME(UTC): 2023-07-04 13:57:40
PRODUCT CREATE END TIME(UTC)   : 2023-07-04 13:57:40
FILESIZE (BYTES)               : 21086440
FILENAME                       : AOD1B_2012-05-01_X_07.asc
PROCESS LEVEL (1A OR 1B)       : 1B
PRESSURE TYPE (SP OR VI)       : VI
MAXIMUM DEGREE                 : 180
COEFFICIENT ERRORS (YES/NO)    : NO
COEFF. NORMALIZED (YES/NO)     : YES
CONSTANT GM [M^3/S^2]          :  0.39860044180000E+15
CONSTANT A [M]                 : 0.63781366000000E+07
CONSTANT FLAT [-]              :  0.29825642000000E+03
CONSTANT OMEGA [RAD/S]         : 0.72921150000000E-04
NUMBER OF DATA SETS            : 32
DATA FORMAT (N,M,C,S)          : (2(I3,X),E15.9,X,E15.9)
END OF HEADER
DATA SET 01:   16471 COEFFICIENTS FOR 2012-05-01 00:00:00 OF TYPE atm
  0   0 0.267376895E-10 0.000000000E+00
  1   -.175641539E-09 0.000000000E+00
...
DATA SET 02:   16471 COEFFICIENTS FOR 2012-05-01 00:00:00 OF TYPE ocn
  0   0 -.134868436E-12 0.000000000E+00
  1   0 -.151138849E-10 0.000000000E+00
...
DATA SET 03:   16471 COEFFICIENTS FOR 2012-05-01 00:00:00 OF TYPE glo
  0   0 0.266028211E-10 0.000000000E+00
  1   0 -.190755423E-09 0.000000000E+00
...
DATA SET 04:   16471 COEFFICIENTS FOR 2012-05-01 00:00:00 OF TYPE oba
  0   0 0.457209337E-09 0.000000000E+00
  1   0 -.392380502E-10 0.000000000E+00
...
```

Appendix B

AOe07 Format Description and Download

The error time-series for AOD1B RL07 is available via the ESA ESM repository under ftp://ig2-dmz.gfz-potsdam.de/ESAESM/.

Format and content of the **error estimation of AOD1B RL07** are described in the following. The files are provided as yearly gzipped tarballs that follow the naming convention "mtm_YYYY_VERSION.tar.gz", where "YYYY" is the year and "VERSION" is the version of the error estimation represents (either "AOe07" as representative for RL07 or the previous version "AOerr" as representative for RL05 and RL06 for AOD1B).

Each yearly archive contains individual files that correspond to one time-step grouped into subfolders for each month of the year. The individual files follow the naming convention: "mtmshc_VERSION_YYYYMMDD_HH.180". Here "VERSION" is again either "AOe07" or "AOerr", "YYYYMMDD" represents the date of the time-step and "HH" the time of day. The extension ".180" signifies the maximum d/o up to which the Stokes coefficients are provided and is fixed to 180.

Each file consists of a header that ends with the line "end_of_head". The lines of the header contain the following information:

`product type`	: anomalous gravity potential
`modelname`	: name of the model
`model content`	: name of the data-set, either AOe07 or AOerr
`version`	: version of the release
`earth_gravity_constant`	: GM value used for computation
`radius`	: semi-major axis value used for computation
`max_degree`	: maximum degree of the spherical harmonic series, here 180
`error`	: yes, if errors are given for each coefficient
`norm`	: yes, if the coefficients are normalized
`tide_system`	: used tidal signals

The following is an example for a single AOe07 product file, where for simplification only the two first coefficients of each data set are given:

```
product type            anomalous gravity potential
modelname               Improved Mass Transport Model
model content           AOe07
version                 1.0
```

```
earth_gravity_constant  0.39860050000000D+15
radius                  6378137.0000
max_degree              180
error                   no
norm                    fully_normalized
tide_system             does-not-apply
end_of_head
gfc    0    0 -0.57090320226609D-11  0.00000000000000D+00
gfc    1    0  0.63387691978226D-12  0.00000000000000D+00
...
```

Appendix C

Error VCM Format Description and Download

The error-variance-covariance matrix based on the AOe07 time-series is available under the DOI https://doi.org/10.5880/nerograv.2023.004.

The repository contains separate ASCII-files for the diagonal variance matrix as well as the fully populated covariance matrix. Each file consists of a header with a dedicated number of lines (NUMBER OF HEADER RECORDS) and ends with a constant header line (END OF HEADER). The header lines are adapted from the AOD1B file structure but only include relevant lines. The first part is based on the Level-1 instrument product header convention (Case *et al.*, 2002) and gives more general information on the product (header lines PRODUCER AGENCY to FILENAME). These lines are followed by a number of header lines describing the VCM mode precisely:

```
PRESSURE TYPE (ATM OR OCN)      : atmospheric pressure orography or ocean bottom pressure
MAXIMUM DEGREE                  : maximum degree of the spherical harmonic series
COEFF. NORMALIZED (YES/NO)      : yes, if the coefficients are normalized
CONSTANT GM [M^3/S^2]           : GM value used for computation
CONSTANT A [M]                  : semi-major axis value used for computation
NUMBER OF DATA SETS             : number of data fields per product file
FORMAT (L1,M1,L2,M2,COV(coeff)): format string to read the data
```

The NUMBER OF DATA SETS is in both cases 1. The MAXIMUM DEGREE is either 180 for the diagonal variance matrix or 40 for the fully populated VCM.

More detailed information on the structure of the files including the ordering of the coefficients is given in the dedicated Technical Note that is provided within the repository.

Appendix D

Acronyms

AOD1B	Atmosphere and Ocean De-Aliasing Level-1B Product
AOe07	Atmosphere and ocean error time-series adapted for AOD1B RL07
CHAMP	Challenging Minisatellite Payload
CM frame	Center of Mass of the Earth System isomorphic frame
ECMWF	European Centre for Medium-Range Weather Forecasts
ERA5	ECMWF Re-Analysis 5
GFZ	Deutsches GeoForschungsZentrum - German Research Centre for Geosciences
GOCE	Gravity Field and Steady-State Ocean Circulation Explorer
GRACE	Gravity Recovery And Climate Experiment
GRACE-FO	Gravity Recovery And Climate Experiment Follow-On
HOPE	Hamburg Ocean Primitive Equation Model
IB	Inverse Barometer
IERS	International Earth Rotation and Reference Systems Service
IFS	Integrated Forecasting System of the ECMWF
ISDC	Information System and Data Center at GFZ
JPL	Jet Propulsion Laboratory
LAGEOS	Laser Geodynamics Satellite or Laser Geometric Environmental Observation Survey
LRI	Laser Ranging Interferometer
LSG	Large-Scale Geostrophic Model
NWP	Numerical Weather Prediction
MERRA2	Modern-Era Retrospective analysis for Research and Applications,Version 2
MPIOM	Max-Planck-Institute for Meteorology Ocean Model
OBP	Ocean Bottom Pressure
OGCM	Ocean General Circulation Model
OMCT	Ocean Model for Circulation and Tides
PPHA	Barotropic ocean model code named after its main developers R. Pacanowski, R. Ponte, N. Hirose, and A. Ali
SAL	Self-Attraction and Loading
TiME	Tidal Model forced by Ephemerides
VCM	Variance-Covariance Matrix
WMO	World Meteorological Organization